

22 **ABSTRACT**

23 In dividing cells, depolymerizing spindle microtubules move chromosomes by pulling at
24 their kinetochores. While kinetochore subcomplexes have been studied extensively *in*
25 *vitro*, little is known about their *in vivo* structure and interactions with microtubules or
26 their response to spindle damage. Here we combine electron cryotomography of serial
27 cryosections with genetic and pharmacological perturbation to study the yeast
28 chromosome-segregation machinery at molecular resolution *in vivo*. Each kinetochore
29 microtubule has one (rarely, two) Dam1C/DASH outer-kinetochore assemblies.
30 Dam1C/DASH only contacts the flat surface of the microtubule and does so with its
31 flexible “bridges”. In metaphase, 40% of the Dam1C/DASH assemblies are complete
32 rings; the rest are partial rings. Ring completeness and binding position along the
33 microtubule are sensitive to kinetochore attachment and tension, respectively. Our
34 study supports a model in which each kinetochore must undergo cycles of
35 conformational change to couple microtubule depolymerization to chromosome
36 movement.

37 INTRODUCTION

38 The spindle apparatus, a microtubule-based machine, partitions chromosomes equally
39 between mother and daughter cells during mitosis. In yeast, the microtubules (MTs) in
40 both the nucleus and cytoplasm are anchored by their closed “minus” ends to the
41 nuclear-envelope-embedded microtubule-organizing centers, termed spindle pole
42 bodies. The MT “plus” end (the tips of the 13 protofilaments) can have either a flared or
43 ‘ram’s horn’ configuration (Winey et al., 1995). Kinetochore MTs (kMTs) attach to
44 chromosomes while the long pole-to-pole MTs render the spindle its characteristic
45 shape. To prevent chromosome missegregation, cells employ the spindle assembly
46 checkpoint (SAC) to delay anaphase onset until two conditions are met: first, each sister
47 chromosome must attach to kMTs emanating from one of the spindle pole bodies (bi-
48 orientation or amphitelic attachment) (Musacchio and Salmon, 2007). Second, the
49 spindle must generate tension via opposition between the kMT-induced poleward
50 pulling forces and the cohesion between sister chromatids mediated by cohesin
51 complexes (Michaelis et al., 1997). Damaged spindles and erroneous kMT attachments
52 resulting in either unoccupied kinetochores or a loss of tension in the spindle apparatus
53 leads to the activation of the SAC. The activated SAC imposes a transient cell-cycle
54 arrest in prometaphase, allowing cells to restore kinetochore-microtubule attachments
55 before progressing to anaphase (Tanaka, 2010).

56 The kinetochore is a multi-functional protein complex that mediates the
57 chromosome-kMT attachment and couples kMT depolymerization to poleward
58 movement of the chromosome. Furthermore, the kinetochore is central to the SAC
59 because it can assess the quality of chromosome-kMT attachment. Kinetochores are so

60 complex that its subassemblies -- classified as centromere-proximal “inner-kinetochore”
61 or kMT-associated “outer-kinetochore” complexes based on traditional EM studies -- are
62 often studied as reconstituted complexes (Musacchio and Desai, 2017). High-precision
63 fluorescence imaging *in vivo* has revealed the composition and the average positions of
64 many of these subassemblies (Joglekar and Kukreja, 2017). In yeast, the best-
65 understood one is the outer-kinetochore Dam1C/DASH complex (Cheeseman et al.,
66 2001; Hofmann et al., 1998; Janke et al., 2002; Jones et al., 1999; Li et al., 2002). Ten
67 different polypeptides assemble as a Dam1C/DASH heterodecamer (Miranda et al.,
68 2005). Dam1C/DASH heterodecamers can further oligomerize as rings around MTs
69 (Miranda et al., 2005; Westermann et al., 2005). Owing to their circular shape and ability
70 to form stable load-bearing attachments on MTs *in vitro* (Asbury et al., 2006; Franck et
71 al., 2007; Westermann et al., 2006), Dam1C/DASH rings are thought to anchor the
72 chromosome onto kMTs and couple kMT depolymerization to chromosomal poleward
73 movement by interacting with the protofilaments’ curved tips (Efremov et al., 2007).

74 Knowledge of kinetochore structure at the molecular level *in vivo* would shed light
75 on fundamental questions that cannot be addressed by reconstitution. These questions
76 include how the kinetochores couple to the kMTs; how the kinetochore subunits are
77 oligomerized; how kinetochores are distributed in 3-D within the spindle; and how both
78 the kinetochore and spindle respond to perturbation. These structural details remain
79 largely unknown *in vivo* because kinetochores are sensitive to conventional electron-
80 microscopy sample-preparation methods (McEwen et al., 1998; McIntosh, 2005).
81 Structural insights into large complexes like kinetochores and spindles *in vivo* require

82 electron cryotomography (cryo-ET), which can reveal the 3-D architecture of giant
83 cellular machines and their subcomponents in a life-like state (Gan et al., 2011).

84 We used cryo-ET of both serial and single frozen-hydrated sections
85 (cryosections) to test decades-old structural models of the yeast chromosome-
86 segregation system *in vivo*. We have examined the structure of yeast outer-kinetochore
87 Dam1C/DASH oligomers and their interactions with kMT walls in metaphase cells both
88 with and without tension, in cells treated with a spindle poison, and in comparison to
89 Dam1C/DASH-MT complexes *in vitro*. We found that Dam1C/DASH can oligomerize
90 into two types of rings, both of which can stably associate with kMTs. Finally, our study
91 reconciles different views concerning the mechanism of outer-kinetochore function in a
92 new model of MT-powered chromosome movement.

93 **RESULTS**

94

95 **Dam1C/DASH forms both complete and partial rings *in vitro***

96 To understand how individual Dam1C/DASH rings interact with MTs, we performed
97 cryo-ET of plunge-frozen Dam1C/DASH assembled around MTs *in vitro* (Fig. S1)
98 (Miranda et al., 2005). We observed both complete and partial rings (Fig. 1A-B).
99 Consistent with previous studies (Miranda et al., 2005; Westermann et al., 2005), our
100 cryotomograms showed that most Dam1C/DASH rings are slightly tilted relative to the
101 MT's axis. Furthermore, most of these complete and partial rings have flexible
102 structures that connect the ring's rim to the MT walls (Fig. 1C). These connections are
103 called "bridges" (Miranda et al., 2007; Wang et al., 2007; Westermann et al., 2005) and
104 are thought to be composed of parts of the Dam1p and Duo1p proteins (Legal et al.,
105 2016; Zelter et al., 2015).

106 Rotational power-spectra analyses (Murphy et al., 2006) of individual rings
107 showed that most of the complete Dam1C/DASH rings had 17-fold symmetry *in vitro*
108 (Fig. S2A-G). This conclusion was further supported by asymmetric 3-D class averages,
109 which also have 17-fold symmetry (Fig. 1D and S3). Unlike in previous studies (Ramey
110 et al., 2011; Wang et al., 2007; Westermann et al., 2006), we did not observe any 16-
111 fold-symmetric rings *in vitro*; the reason for this difference is not clear. Nevertheless, our
112 Dam1C/DASH structure shares similar motifs with the previous ring structure (Ramey et
113 al., 2011), such as the inward-pointing stump-like densities that correspond to a portion
114 of the bridge (Fig. 1E) and densities extending from the ring's rim, parallel with the MT
115 surface. We call these latter motifs "protrusions", following the nomenclature of a recent

116 structure of reconstituted Dam1C/DASH rings (Steve Harrison, personal
117 communication). For brevity, herein we use the terms bridge, rim, and protrusion when
118 referring to these prominent Dam1C/DASH structural motifs (Fig. 1E).

119

120 **Strategy to study yeast kinetochore structure *in vivo***

121 The *in vivo* structure of Dam1C/DASH is unknown. Previous tomography studies of
122 high-pressure-frozen, freeze-substituted cells revealed weak densities at kMT plus ends
123 that might be partial or complete rings (McIntosh et al., 2013). To eliminate fixation,
124 dehydration and staining as sources of structural distortion, we prepared all our cells by
125 high-pressure freezing, followed by thinning to ~ 100 - 150 nm by cryomicrotomy. As a
126 positive control, we assembled Dam1C/DASH rings around MTs *in vitro* and subjected
127 these samples to the same high-pressure freezing and cryomicrotomy done for cells.
128 The contrast of cryotomograms from such samples is extremely low due to the high
129 concentration of the dextran cryoprotectant (Chen et al., 2016). Both partial and
130 complete Dam1C/DASH rings were nevertheless visible in the resultant cryotomograms
131 (Fig. S4). Therefore, cryo-ET of cryosections can reveal both partial and complete
132 Dam1C/DASH rings around kMTs if they exist *in vivo*.

133 We prepared mitotic yeast cells with either attached kinetochores under tension,
134 detached kinetochores without tension, or attached kinetochores without tension (Fig.
135 2A). Knockdown of Cdc20 function causes yeast cells to arrest in metaphase with
136 kinetochores attached to the spindle and under tension (Lau and Murray, 2012; O'Toole
137 et al., 1997). To visualize kinetochores in metaphase, we arrested cells by depleting
138 Cdc20 in a GAL-Cdc20 strain (Fig. 2B). Because kinetochores take up a tiny fraction of

139 the cell's volume, a single cryosection taken randomly through a cell is unlikely to
140 contain a kinetochore. To overcome this challenge, we devised a parallel-bar-grid-
141 based serial-cryo-ET workflow that made possible the reconstruction of larger portions
142 of spindles (Fig. 2C and D, 3A).

143

144 **Dam1C/DASH forms both complete and partial rings around kMTs *in vivo***

145 We reconstructed portions of 23 metaphase spindles, each with at least 3 serial
146 cryotomograms (most-complete example in Fig. S5). We identified kMTs based on their
147 short length, location, and orientation relative to the nuclear envelope (Fig. 3B). Both
148 complete and partial ring structures encircled the kMT plus ends (Fig. 3C-F). We herein
149 assign these complete and partial rings as Dam1C/DASH because their shape,
150 diameter (47 ± 5 nm, mean and standard deviation, $n = 12$), localization at the kMT
151 plus-ends, bridge densities (see below), and their absence from cytoplasmic MTs (see
152 below) are all consistent with that expected of Dam1C/DASH from *in vivo* and *in vitro*
153 studies. Our most complete serial-cryo-ET reconstruction (Figs. 3B and S5) contained
154 half a spindle with 13 Dam1C/DASH rings (Fig. 3B). Budding yeast cells have 16
155 kinetochores per half spindle (one kinetochore per sister chromosome), so we probably
156 missed 3 Dam1C/DASH rings due to the ambiguity of cryo-ET densities near the
157 cryosection surfaces (14 surfaces in 7 cryosections). The reconstruction is complete
158 enough that we estimate that all kinetochores would fit into a rectangular volume less
159 than $0.5 \mu\text{m}$ on a side (Fig. 3C).

160

161 **Dam1C/DASH bridges contact the flat or gently curved surfaces of kMTs**

162 Most kMTs had a single Dam1C/DASH ring (complete or partial, $n = 82$) (Fig. 3B and
163 C). Only 4 kMTs had two partial Dam1C/DASH rings each (one example shown in Fig.
164 3C). All rings were tilted relative to the kMT axis and the majority of them were
165 positioned within 50 nm of the plus end. We did not observe any contacts between
166 Dam1C/DASH and the protofilaments' curved tips. Instead, the only Dam1C/DASH-kMT
167 interactions observed were between the kMT walls and Dam1C/DASH's bridges (Fig.
168 3D-F; additional examples in Fig S6). Furthermore, we did not observe any contact
169 between Dam1C/DASH and the back of the protofilaments' curve tips *in vitro* (Fig. S7).
170 The Dam1C/DASH bridges are conformationally heterogeneous, even within the same
171 ring, and could either be coplanar with the rim or curved out of plane (Fig. 3D and E). If
172 each Dam1C/DASH heterodecamer contributes a single bridge, then there would be up
173 to 17 bridges per ring. In both our *in vivo* and *in vitro* datasets, we observed up to 8
174 bridges per ring, meaning that most of the bridges were in an as-yet-unknown
175 conformation. This conformational flexibility explains how the bridge appears as a
176 continuous density from the Dam1C/DASH rim to the MT surface in cryotomograms but
177 as a stump-like density in multi-ring averages.

178 Two complete Dam1C/DASH rings *in vivo* had sufficient contrast to reveal that
179 they had 17-fold symmetry (one analysis shown in Fig. S2H). To better understand how
180 Dam1C/DASH is organized *in vivo*, we symmetrized these two rings, yielding density
181 maps with higher signal-to-noise-ratio (Fig. 3G). These symmetrized rings have
182 protrusions, which extend from the rim like the rings *in vitro* (Fig. 1D). In both instances,
183 the protrusions point toward the kMT plus end, possibly as a result of interactions with
184 other kinetochore proteins. The surface opposite the protrusions is relatively

185 featureless, similar to the rings seen *in vitro*. From these symmetrized rings, we
186 estimate that partial rings missing four or more Dam1C/DASH heterodecamers would
187 have a gap large enough for a MT to pass through them (Fig. 3G).

188

189 **Unattached Dam1C/DASH forms partial rings, which remain clustered**

190 Damaged spindles activate the SAC and can cause kinetochore detachment (Gillett et
191 al., 2004). To test how spindle disruption affects kinetochore organization, we treated
192 Dam1p-GFP-expressing cells with the spindle poison nocodazole and then imaged
193 them by immunofluorescence microscopy (Fig. 4A). Excluding a small subset of cells
194 that lacked both Dam1C/DASH and MT fluorescence signals, cells had either zero
195 (18%, n = 41), one (63%, n = 143), or two punctate tubulin signals (13%, n = 30).
196 Punctate MT fluorescence signals suggests that they are very short and form small
197 clusters. Unlike MTs, all Dam1C/DASH fluorescence was confined to a single focus,
198 suggesting that all the Dam1C/DASH rings formed a single cluster.

199 The intact spindle is a prominent landmark that facilitated our systematic search
200 for kinetochores in metaphase-arrested cells; this strategy was not possible in
201 nocodazole-treated cells because spindles are disrupted. We therefore performed cryo-
202 ET of 131 randomly chosen cryosections of these cells and were able to locate kMTs in
203 5 cryotomograms. Consistent with the immunofluorescence data, the nocodazole-
204 treated cells contained small clusters of extremely short MTs (20 - 50 nm long, Fig. 4B
205 and Table S1), all of which had flared ends. In untreated cells, cytoplasmic MTs have
206 their plus ends near the cell membrane, making them extremely challenging to find in
207 cryosections. Owing to their shortness in nocodazole-treated cells, the plus ends of four

208 cytoplasmic MTs were seen in the vicinity of the nuclear envelope. Dam1C/DASH rings
209 were found around some kMTs (nuclear) while cytoplasmic MTs did not have any
210 Dam1C/DASH rings encircling them (Fig. 4B-D). In one instance, we observed the
211 Dam1C/DASH rim in contact with the kMT surface (Fig. 4D), but we did not see any
212 Dam1C/DASH rings contacting the back of the protofilaments' curved tips. Like in
213 metaphase cells, Dam1C/DASH rings attached to kMT walls via flexible bridges. We
214 also located small clusters of unattached Dam1C/DASH partial rings in the
215 nucleoplasm, far from the spindle pole body (Fig. 4E and F). Our observations are
216 consistent with the notions that kinetochores are clustered by an MT-independent
217 mechanism (Goshima and Yanagida, 2000; Jin et al., 2000; Richmond et al., 2013) and
218 that all sixteen budding-yeast kinetochores work together like a single, much-larger
219 mammalian kinetochore (Aravamudhan et al., 2014; Joglekar et al., 2009; Joglekar et
220 al., 2008). In summary, some Dam1C/DASH subcomplexes detach from damaged
221 spindles and are found as clusters of partial rings. Another subset of Dam1C/DASH
222 rings encircle the extremely short kMTs and only contact the kMT's flat surface.

223

224 **Kinetochore position on the kMT is sensitive to tension**

225 Even if kinetochores are attached to kMTs, the spindle checkpoint can still be activated
226 if tension across the spindle is lost. To determine how the outer kinetochore responds to
227 loss of tension in the presence of attached kinetochores, we imaged metaphase cells in
228 which cohesin can be conditionally cleaved. In these cells, Scc1 is replaced by Scc1-
229 TEV268, which can be cleaved at an internal recognition site by inducible TEV protease
230 (Mirchenko and Uhlmann, 2010; Uhlmann et al., 2000) (and this paper). Light

231 micrographs showed that these cells have a large bud, extra-long spindle, and a multi-
232 lobed nucleus (Fig. 5A). Our cryotomograms confirmed that these cells had distorted
233 nuclei and showed that MTs were absent from the center of the spindle (Fig. 5B and
234 S8). We located 33 Dam1C/DASH rings, which were much more difficult to find because
235 longer kMTs made the plus ends rarer in our cryotomograms and because many rings
236 were located far from the kMT plus end (example serial reconstruction in Fig. 5C and
237 Table S1). Unlike in the other cells we imaged, Dam1C/DASH rings were rarely
238 clustered; only one such cluster was found in this dataset (Fig. S8). The ratio of
239 complete to partial rings in these cells was similar to that in metaphase cells (Table S1).

240 In the absence of tension, some Dam1C/DASH rings were located very far (>
241 100 nm) from the kMT plus ends. To test for a correlation between tension and the
242 location of a Dam1C/DASH ring along a kMT, we measured the kMT-tip-to-
243 Dam1C/DASH distance for all three spindle conditions, with complete and partial rings
244 kept as separate groups (Fig. 5E). In metaphase cells with kinetochores under tension,
245 there was no difference between the kMT-tip-to-Dam1C/DASH distances in complete
246 and partial rings (means and standard deviations -- complete ring: 17 ± 18 nm, $n = 17$;
247 partial ring: 24 ± 18 nm, $n = 26$; two-tailed t-test $p > 0.05$). However, in the absence of
248 spindle tension, a few partial rings were located much farther from the kMT plus ends
249 than the complete rings (complete ring: 17 ± 6 nm, $n = 4$; partial ring: 82 ± 80 nm, $n = 6$;
250 F-test, $p < 0.01$). The complete rings in all three spindle states -- metaphase,
251 tensionless, disrupted -- were located close to the kMT plus end (disrupted spindle: $12 \pm$
252 6 nm, $n = 7$, two-tailed t-test $p > 0.05$ for all pairwise comparisons). In summary,

253 complete rings, but not partial rings, remain associated with the kMT plus end in the
254 absence of tension.

255 **DISCUSSION**

256 The discovery that the Dam1C/DASH outer-kinetochore complex can form rings around
257 MTs suggested a mechanism for how kinetochores can remain attached to a dynamic
258 kMT tip (Hill, 1985; Miranda et al., 2005). Notably, a kMT-encircling complete ring is
259 thought to be topologically trapped because its means of dissociation is the plus end,
260 which is blocked by the protofilaments' curved tips. Structural studies have revealed a
261 more complicated picture: Dam1C/DASH can also form spirals and partial rings (Gonen
262 et al., 2012; Wang et al., 2007). Furthermore, calibrated fluorescence-microscopy
263 experiments revealed that each kinetochore has, on average, twelve Dam1C/DASH
264 heterodecamers (Dhatchinamoorthy et al., 2017), challenging the notion that the
265 complete ring is the only functional form of Dam1C/DASH *in vivo*. Our study has now
266 shown that partial and complete partial Dam1C/DASH rings coexist *in vivo*, with partial
267 rings being the majority species. Many partial rings have gaps larger than 25 nm,
268 meaning that those kinetochores do not attach to kMTs by topological means. How
269 would Dam1C/DASH keep chromosomes attached to spindles under tension? We
270 believe that the bridge-kMT interactions *in vivo* are more stable than previously
271 appreciated. In support of this notion, single-molecule studies suggested that
272 Dam1C/DASH oligomers with only one to four heterodecamers, which are not
273 topologically trapped on a MT, can be pulled by depolymerizing MT plus ends (Gestaut
274 et al., 2008). Such stable interactions would be consistent with the observation that the
275 MT-bound Dam1C/DASH pool does not exchange freely with the nucleoplasmic pool
276 (Dhatchinamoorthy et al., 2017).

277

278 **Dam1C/DASH is sensitive to both tension and attachment**

279 Spindle integrity and tension at the kinetochore are thought to influence kinetochore
280 structure, leading to SAC signaling. We have experimentally damaged the spindle of
281 some cells and eliminated tension at the kinetochore of others. Our resultant analysis
282 reveals that outer-kinetochore is sensitive to both attachment and tension in these
283 mitotically arrested cells. Dam1C/DASH's oligomerization state *in vivo* depends on
284 attachment but not tension (Fig. 6A and Table S1). The kinetochore's position along the
285 kMT's length is more complicated: they are located near the plus end unless there is no
286 tension and the Dam1C/DASH ring is a partial one. How might these oligomerization
287 and positioning differences be related to the SAC? An early fluorescence-microscopy
288 study showed that in nocodazole-treated cells, kinetochores far from the spindle pole
289 body, but not those nearby, recruited checkpoint proteins (Gillett et al., 2004). Our
290 cryotomograms suggest that in nocodazole-treated cells, checkpoint-protein-associated
291 kinetochores have detached partial Dam1C/DASH rings while the "checkpoint-silent"
292 kinetochores are still attached to short kMTs in the spindle remnant and have complete
293 rings. The causal relationship between the SAC and the Dam1C/DASH phenotypes *in*
294 *vivo* remain to be determined.

295

296 **The yeast kinetochore is not a monolithic structure**

297 Dam1C/DASH interacts with the KMN (Knl1, Mtw1, Ndc80) outer-kinetochore network
298 and other kinetochore proteins, many of which have long coiled-coil domains (Caldas
299 and DeLuca, 2014; Wang et al., 2008; Westermann et al., 2005). Such extended
300 structures are skinny and would have been missed in our cryotomograms. However,

301 globular domains such as the Ndc80 calponin-homology domain may account for some
302 of the small densities protruding from kMT plus ends (Fig. 3E). In the vicinity of the kMT,
303 there are also many nucleosome-sized densities, some of which may account for the
304 centromeric nucleosome or the center of the hub-shaped MIND (Mtw1, Nnf1, Nsl1,
305 Dsn1) complex (Dimitrova et al., 2016; Gonen et al., 2012; Tachiwana et al., 2011). Of
306 these complexes, the centromeric nucleosome is expected to be coaxial with the kMT
307 (McIntosh et al., 2013), but we did not observe any enrichment of nucleosome-size
308 densities along this axis. Instead, the majority of the kinetochores probably bind kMTs
309 off-axis *in vivo*, which is a phenotype of purified kinetochores (Gonen et al., 2012). Our
310 cryotomograms are consistent with a model in which the yeast kinetochore is a highly
311 flexible structure and with its mass spread over a large volume (Dimitrova et al., 2016)
312 (Steve Harrison, personal communication].

313

314 **A model for microtubule-driven chromosome movement**

315 Yeast chromosomes move poleward along kMTs by two different mechanisms. Newly
316 assembled yeast kinetochores first contact the side of a kMT and slide poleward by
317 means of the kinesin Kar3 (Tanaka et al., 2005). Eventually, the kMT plus end contacts
318 the kinetochore, leading to an “end-on” interaction and kMT-driven chromosome
319 poleward movement (Kitamura et al., 2007; Tanaka et al., 2007; Tanaka et al., 2005).
320 There are two popular models of kMT-driven chromosome poleward movement. In the
321 ratchet model (Hill, 1985), kinetochores attach to the spindle by numerous weak
322 interactions and undergo a random walk along kMTs, but have biased poleward
323 movement by the receding plus end. In the forced-walk model (Efremov et al., 2007),

324 the depolymerizing protofilaments push a strongly bound kinetochore and force it to
325 slide poleward. We did not observe any instance of Dam1C/DASH in contact with the
326 protofilaments' curved tips in any of the three conditions. Contact between
327 Dam1C/DASH and the protofilaments' curved tips must therefore be transient. We did
328 frequently observe contacts between the Dam1C/DASH bridge and the MT's flat
329 surface. To explain these observations, we propose a model that incorporates ideas
330 from both the forced-walk and ratchet models (Fig. 6B). Steps 1 - 2: Once the kMT
331 surface underneath Dam1C/DASH becomes curved enough, bridge detachment is
332 triggered. Step 3: If a sufficient number of Dam1C/DASH heterodecamers lose contact,
333 then the Dam1C/DASH ring can diffuse. Step 4, equivalent to step 1: Once the
334 Dam1C/DASH ring translates to a position where straight protofilaments are available,
335 its bridges can reattach. As the kMT shortens, Dam1C/DASH heterodecamers must
336 cycle between attached and detached states, biased poleward by transient steric
337 interactions between Dam1C/DASH and protofilament curved tips. Human kinetochores
338 may also use this kMT-driven segregation mechanism if the functional homolog of
339 Dam1C/DASH, called Ska1 (Abad et al., 2014; Hanisch et al., 2006; Janczyk et al.,
340 2017; van Hooff et al., 2017; Welburn et al., 2009; Zhang et al., 2017), can switch
341 rapidly between bound and unbound states.

342 **MATERIALS AND METHODS**

343

344 **Cell strains**

345 All strains used in this study are detailed in Table S2.

346

347 **Cell culture and metaphase arrest**

348 Strain US1375 was grown in 50 ml YEPG (YEP: 10% yeast extract, 20% peptone,

349 supplemented with 2% galactose and 2% raffinose) at 30°C, 250 RPM, to mid-log

350 phase ($OD_{600} = 0.5 - 1.0$) before a change of growth medium to YEPD (YEP with 2%

351 glucose). All growth-medium changes were done by draining YEPG with a vacuum filter,

352 washing with twice the volume of YEPG, and then resuspending the cells in YEPD.

353 Next, the cells were kept in YEPD at 30°C for 3 hours to arrest at metaphase. Right

354 before self-pressurized freezing, the cells were checked by light microscopy for signs of

355 large buds, which indicates successful metaphase arrest.

356

357 **Metaphase arrest without cohesion**

358 Strain US4780 was grown in YEPD without methionine overnight, then arrested in G1

359 phase by addition of alpha factor to 5 $\mu\text{g/ml}$. The cells were then washed free of alpha

360 factor and then arrested at metaphase by incubation in YEP + raffinose + methionine

361 medium for 4.5 hours. Metaphase-arrested cells were then incubated in YEPG for 1.5

362 hours to induce TEV protease expression.

363

364 **Nocodazole arrest**

365 Strains US1363 and US8133 were grown overnight in YEPD before arresting at G1
366 phase by incubation in YEPD containing 0.8 µg/ml alpha factor for 3 hours. The arrested
367 cells were then washed free of alpha factor and released into YEPD containing 15 µg/ml
368 nocodazole. Cells were self-pressurized frozen after 4 hours of incubation.

369

370 **Immunofluorescence**

371 Yeast cells were collected by pelleting 1 ml of liquid culture at 15,000 x g for 1 minute.
372 The pellet was then fixed in KPF (100 mM K₂HPO₄, 4% paraformaldehyde) at 22°C for
373 1.5 hours. The cells were then washed three times with 1 ml 100 mM K₂HPO₄, then
374 once with 1 ml SB (1.2 M sorbitol, 100 mM phosphate-citrate). Next, the cells were
375 incubated at 30°C in 200 µl SB containing glucanase and zymolase for cell wall
376 digestion. The resulting spheroplasts were washed with SB and then incubated with
377 primary antibody (diluted 1:1000) for 2 hours at 22°C. After washing out the unbound
378 primary antibody with BSA-PBS (1% BSA, 40 mM K₂HPO₄, 10 mM KH₂PO₄, 150 mM
379 NaCl), the spheroplasts were incubated with secondary antibody (diluted 1:2000) for 2
380 hours at 22°C. After washing out excess secondary antibody with BSA-PBS, the
381 spheroplasts were suspended in 5 µl of mounting media (Vectashield H-1200, Vector
382 Laboratories, Burlingame, CA) and imaged using a Perkin Elmer spinning disc confocal
383 microscope.

384

385 **Dam1C/DASH expression, purification and assembly**

386 Dam1C/DASH heterodecamers were expressed and purified using slightly modified
387 published protocols (Miranda et al., 2005; Westermann et al., 2005). All protein buffers

388 contained protease inhibitor (cOmplete, Sigma, St. Louis, MO). The plasmid
389 pC43HSK3H (Miranda et al., 2005) was transformed into BL21 Rosetta 2 (DE3) pLysS
390 cells. This plasmid expresses all ten Dam1C/DASH polypeptides (Dam1p, Dad1p,
391 Dad2p, Dad3p, Dad4p, Duo1p, Ask1p, Spc19p, Spc34p, Hsk3p). Cells were grown to
392 OD₆₀₀ = 0.4, then induced by addition of IPTG to 1 mM. After 4 hours of induction at
393 37°C, the cells were pelleted by centrifugation at 5,000 x g for 15 minutes. The cells
394 were resuspended in 30 ml sonication buffer (20 mM sodium phosphate pH 6.8, 500
395 mM NaCl, 1 mM EDTA, 20 mM Imidazole, 0.5% v/v Triton X-100) and lysed by
396 sonication at 4°C for 5 minutes (power: 500 W, frequency: 20 kHz; amplitude: 35%,
397 pulse: 0.5 s, elapsed: 0.5 s). The lysates were then centrifuged at 15,000 x g for 30
398 minutes to remove the debris. Ni-NTA agarose beads (5 ml) were exchanged into
399 sonication buffer by twice pelleting at 100 x g for 2 minutes, then resuspending in
400 sonication buffer. The Ni-NTA beads were then mixed with the lysates and incubated at
401 4°C for 2 hours. Next, the Ni-NTA beads were pelleted by centrifugation at 2,000 x g for
402 2 minutes and washed with sonication buffer twice. Elution buffer (20 ml) was added
403 into the Ni-NTA beads and rotated overnight at 4°C at 200 RPM. The eluate was
404 centrifuged at 100 x g for 2 minutes. The supernatant was dialyzed to SP low-salt buffer
405 (20 mM sodium phosphate pH 6.8, 150 mM NaCl, 1 mM EDTA) and concentrated to 1
406 ml. The concentrated eluate was loaded into a 1 ml HiTrap SP sepharose cation-
407 exchange column. The fraction that eluted in 600 mM NaCl was further purified by gel
408 filtration in a Superose 6 column in Superose buffer, which also functioned as the
409 Dam1C/DASH storage buffer (20 mM sodium phosphate, pH 6.8, 500 mM NaCl, 1 mM
410 EDTA). The largest peak was concentrated to 1 ml using a Vivaspin concentrator (2 ml)

411 and then aliquoted to 10 μ l per tube. The aliquots were snap frozen with liquid nitrogen
412 and stored at -80°C (Westermann et al., 2005).

413

414 **Preparation of control Dam1C/DASH around MTs**

415 Porcine tubulin (5 mg/ml, T240, Cytoskeleton, Denver, CO) was polymerized into MTs
416 and stabilized with Taxol following a published protocol (Westermann et al., 2005), with
417 modifications. The incubation time was extended to 2 hours. The purified Dam1C/DASH
418 heterodecamers (1 mg/ml) were incubated with Taxol-stabilized MTs (5 mg/ml) for 20
419 minutes at 22°C. For the cryomicrotomy control, purified Dam1C/DASH heterodecamers
420 (2.3 mg/ml) were incubated with Taxol-stabilized MTs (5 mg/ml) for 30 minutes at 22°C.
421 Then, an equal volume of 80% dextran ($M_r \sim 6,000$) was added to the solution and
422 gently mixed before self-pressurized freezing.

423

424 **Plunge freezing and self-pressurized freezing of Dam1C/DASH around MTs**

425 Dam1C/DASH-MT complexes (3 μ l) were applied on the carbon side of a Quantifoil 2/2
426 grid (Quantifoil Micro Tools GmbH, Großlöbichau, Germany). Gold colloids (10-nm, BBI
427 solutions, Cardiff, UK) were added as tomographic alignment fiducials. The colloids (20
428 μ l) were first pelleted and the supernatant was removed. Dam1C/DASH-MT complexes
429 (3 μ l) were then mixed with the gold pellet and applied to the EM grid. The grid was
430 blotted for 2 seconds with force 2 and then plunged in liquid ethane using a Vitrobot
431 (Thermo, Waltham, MA), set to 100% humidity at 4°C.

432

433 **Self-pressurized freezing**

434 Cells and cryomicrotomy control samples were self-pressurized frozen based on a
435 previous protocol (Yakovlev and Downing, 2011). Arrested cells (50 ml) were pelleted at
436 5,000 x g, 4°C for 5 minutes. The pellet was then resuspended in 1 ml of YEPD or
437 YEPG. The cells were re-pelleted at 3,000 x g for 1 minute at 22°C and the supernatant
438 was discarded. Next, the cell pellet was resuspended gently in an equal volume of 50%
439 dextran ($M_r \sim 6,000$). The resulting mixture was drawn into a copper tube (0.45 mm
440 outer diameter) using a syringe-style loading tool (Part 733-1; Engineering Office M.
441 Wohlwend, Sennwald, Switzerland). Both ends of the copper tubes were tightly clamped
442 shut before being dropped into liquid ethane.

443

444 **EM grid preparation for cryosections**

445 Parallel-bar grids (G150PB-CU, EMS, Hatfield, PA) with continuous carbon film were
446 used for serial cryo-ET. The grids were plasma cleaned at 15 mA for 45 seconds. To
447 coat the grids with gold fiducials, the carbon side of the grids were covered with 4 μ l of a
448 solution containing 0.1 mg/ml BSA and 10-nm gold fiducials in water (BBI). The coated
449 grids were air dried overnight then stored in a dry box until use.

450

451 **Cryomicrotomy**

452 All cryomicrotomy was done with a UC7 / FC7 cryomicrotome (Leica Microsystems,
453 Vienna, Austria). The frozen copper tubes were trimmed with a diamond trimming knife
454 (Diatome, Hatfield, PA) until amorphous ice was exposed. The sample was then further
455 trimmed to produce a 130 μ m x 55 μ m x 30 μ m (length x width x height) mesa. Next,
456 100-nm-thick cryosections were cut from the mesa using a 35° diamond knife (Diatome)

457 to produce a cryoribbon, under the control of a micromanipulator (Ladinsky, 2010). The
458 ribbon was picked up using a fiber tool and carefully placed onto an EM grid, parallel to
459 the long bars like in Fig. 1D, and then attached by charging with a Crion device (Leica).
460 A laser window was sometimes used to flatten the cryoribbon on the grid. The grid was
461 then stored in liquid nitrogen until imaged. Owing to sensitivity of serial cryotomography
462 to cell positions being occluded by contaminants, only the grids that had the minimum
463 amount of ice contamination were used. We also devised new cryotools to further
464 minimize ice contamination and facilitate cryomicrotomy (Ng, in preparation).

465

466 **Electron cryotomography of *in vitro* Dam1C/DASH + MT**

467 Tilt series of *in vitro* Dam1C/DASH + MT samples were collected using Tomo4
468 (Thermo). Tilt series of +60° to -60° with an increment of 2° were collected at cumulative
469 dose of 100 - 130 e/Å². For defocus phase-contrast data, the nominal defocus ranged
470 from -10 μm to -14 μm. For Volta phase-contrast data, the nominal defocus was -0.5
471 μm. Tomographic reconstructions were done using the IMOD program *Etomo* (Kremer
472 et al., 1996; Mastronarde, 1997; Xiong et al., 2009). Sequential cryotomograms were
473 joined using *Etomo*.

474

475 **Serial electron cryotomography**

476 Serial cryo-ET data was collected using Tomo4. First, cryosections were imaged at low
477 magnification (2,878 x) to locate positions that showed the nucleus. Next, a single high-
478 magnification (15,678 x) projection image was recorded at a dose sufficient (1 - 2 e/Å²)
479 to determine if that cell position had any spindle MTs. Successive positions centered on

480 the same cell were marked out in the sequential cryosections and saved as targets for
481 tilt series collection. Tilt series of +60° to -60° with an increment of 2° were collected at
482 a cumulative dose of 100 - 130 e/Å². For defocus phase-contrast data, the nominal
483 defocus ranged from -10 to -14 μm. For Volta phase-contrast data, the nominal defocus
484 was -0.5 μm. See Tables S3 and S4 for more details. Tomographic reconstructions and
485 CTF compensation were done using the IMOD program *Etomo* (Kremer et al., 1996;
486 Mastronarde, 1997; Xiong et al., 2009). Sequential cryotomograms were joined using
487 *Etomo*.

488

489 **Tomogram 3-D analysis**

490 MTs in each cryotomogram were located manually and then classified by morphology:
491 plus ends were either blunt, tapered, or had a ram's horn configuration; the MT
492 midsections appeared as tubes; the minus ends were conical. All MT plus-ends were
493 scrutinized for kinetochore structures. To determine the diameter of Dam1C/DASH
494 rings, tomograms were oriented to present the *en face* view of Dam1C/DASH before
495 taking the measurement. To determine distances between kMT plus ends and
496 Dam1C/DASH rings, the tips of kMT plus ends and Dam1C/DASH rings were first
497 treated as two circular disks, then the distance between the center of both disks was
498 taken.

499

500 **Rotational symmetry analysis**

501 Rotational power spectra were estimated using the python script *ot_rot-ps.py*
502 (<https://github.com/anaphaze/ot-tools>). This script calls on EMAN2 routines to calculate

503 correlation coefficients between the original image and copies of the image that were
504 rotated in 1° increments (Tang et al., 2007). This correlation function is then subjected
505 to a 1-D Fourier transform, which can then be inspected for the highest degree of
506 symmetry.

507

508 **Template matching of reconstituted Dam1C/DASH rings**

509 PEET was used to automatically find candidate positions of all ring-shaped
510 macromolecular complexes in cryotomograms of Dam1C/DASH reconstituted on MTs
511 (Heumann, 2016). First, a sparse series of model points were seeded in the lumens of
512 MTs that were encircled by Dam1C/DASH rings. Extra points were then automatically
513 added with Andrew Noske's *curve* tool, implemented in the IMOD program *3dmod*. Two
514 types of reference volumes were tested: 1) a lone featureless 50-nm-diameter ring and
515 2) this same ring encircling a short featureless 25-nm-diameter tube with 4-nm-thick
516 walls. To minimize the effects of densities from the buffer and especially the MTs that
517 protrude beyond the plane of the ring, the subvolumes were masked with a ~ 13-nm-tall,
518 60-nm-diameter cylinder that completely encloses the Dam1C/DASH ring. To assess
519 the performance of the template-matching runs, the "save individual aligned particles"
520 option was enabled in PEET. At the end of the search, overlapping hits were
521 automatically removed by the PEET *removeDuplicates* routine. To minimize the number
522 of false negatives, the correlation-cutoff was set to 0.

523

524 **Subtomogram classification and averaging**

525 Subtomogram analysis was performed using RELION 2.0 and 2.1 with the 2-D and 3-D
526 classification routines (Bharat and Scheres, 2016; Kimanius et al., 2016). The centers of
527 mass of each template-matching hit were imported in RELION. A preliminary round of 2-
528 D classification did not reveal any “junk” classes, e.g., ice crystals, contaminants, and
529 partial rings, probably because the reference model (ring around a short tube) does not
530 resemble the junk classes found in typical cryo-EM samples (Bharat et al., 2015). All
531 template-matching hits were then subjected to 3-D classification, using a featureless 50-
532 nm-diameter ring as an initial reference. The influence of buffer, MT, and nearby
533 Dam1C/DASH densities was minimized by the application of a “soft” edged lifesaver-
534 shaped mask (15-nm thick, with 18- and 30-nm inner and outer radii, respectively). An
535 initial round of asymmetric 3-D classification revealed complete rings highly tilted to
536 various degrees around the MT, partial rings, and spirals; the latter two classes of
537 Dam1C/DASH assemblies were excluded from subsequent analysis. The remaining
538 classes were very similar and had signs of 17-fold rotational symmetry. Dam1C/DASH
539 rings belonging to the class with the clearest 17-fold symmetry were subjected to 3-D
540 autorefinement, using the same mask as before, and with 17-fold symmetry imposed.

541 For *in vivo* subtomogram averaging, the two most complete rings with the
542 strongest 17-fold rotational power were aligned to a featureless 50-nm-diameter ring
543 using PEET. Seventeen-fold symmetry was then enforced with the Bsoft program *bsym*
544 (Heymann and Belnap, 2007). A 12-nm thick ring-shaped mask was applied to eliminate
545 the MT and nearby nucleoplasmic densities.

546

547 **Figures**

548 All cryotomographic slices were generated with the 3dmod *slicer* tool. Isosurface
549 images were rendered with UCSF Chimera (Pettersen et al., 2004). Cartoons and figure
550 layouts were composed with Adobe Illustrator and Photoshop (Adobe Systems, San
551 Jose, CA).

552

553 **Data sharing**

554 The 17-fold-symmetrized subtomogram average of reconstituted Dam1C/DASH rings
555 from Fig. S3A was deposited in the EMDataBank as EMD-6912. The serial
556 cryotomogram that comprise the metaphase spindle from Fig. 3B were deposited in the
557 EMDataBank as EMD-6914. The tilt series for all cryotomograms used to make figures
558 in this paper were deposited in the Electron Microscopy Public Image Archive as
559 EMPIAR-10159.

560 **ACKNOWLEDGEMENTS**

561 We thank the CBIS microscopy staff for support and training, Gemma An for suggesting
562 the use of parallel-bar grids, Shujun Cai for helping with cryo-EM, Simon Jenni and
563 Steve Harrison for Dam1C/DASH plasmids and sharing results prior to publication, Jeff
564 Yong for advice on chromatography, the Jensen lab for computer access, and members
565 of the Gan group, Jack Johnson, Steve Harrison and Paul Matsudaira for feedback.
566 CTN, CC, LD, and LG were funded by NUS startups R-154-000-515-133, R-154-000-
567 524-651, and D-E12-303-154-217, an MOE T2 R-154-000-624-112, with equipment
568 support from NUS YIA R-154-000-558-133. HHL and US were funded by the
569 Biomedical Research Council of A*STAR (Agency of Science Technology and
570 Research), Singapore.

571

572 **Contributions**

573 CTN - experiments, project design, writing, LD - experiments, CC - project design,
574 experiments, HHL - experiments, JS - training, US - project design, writing, LG -
575 experiments, project design, writing.

576 REFERENCES

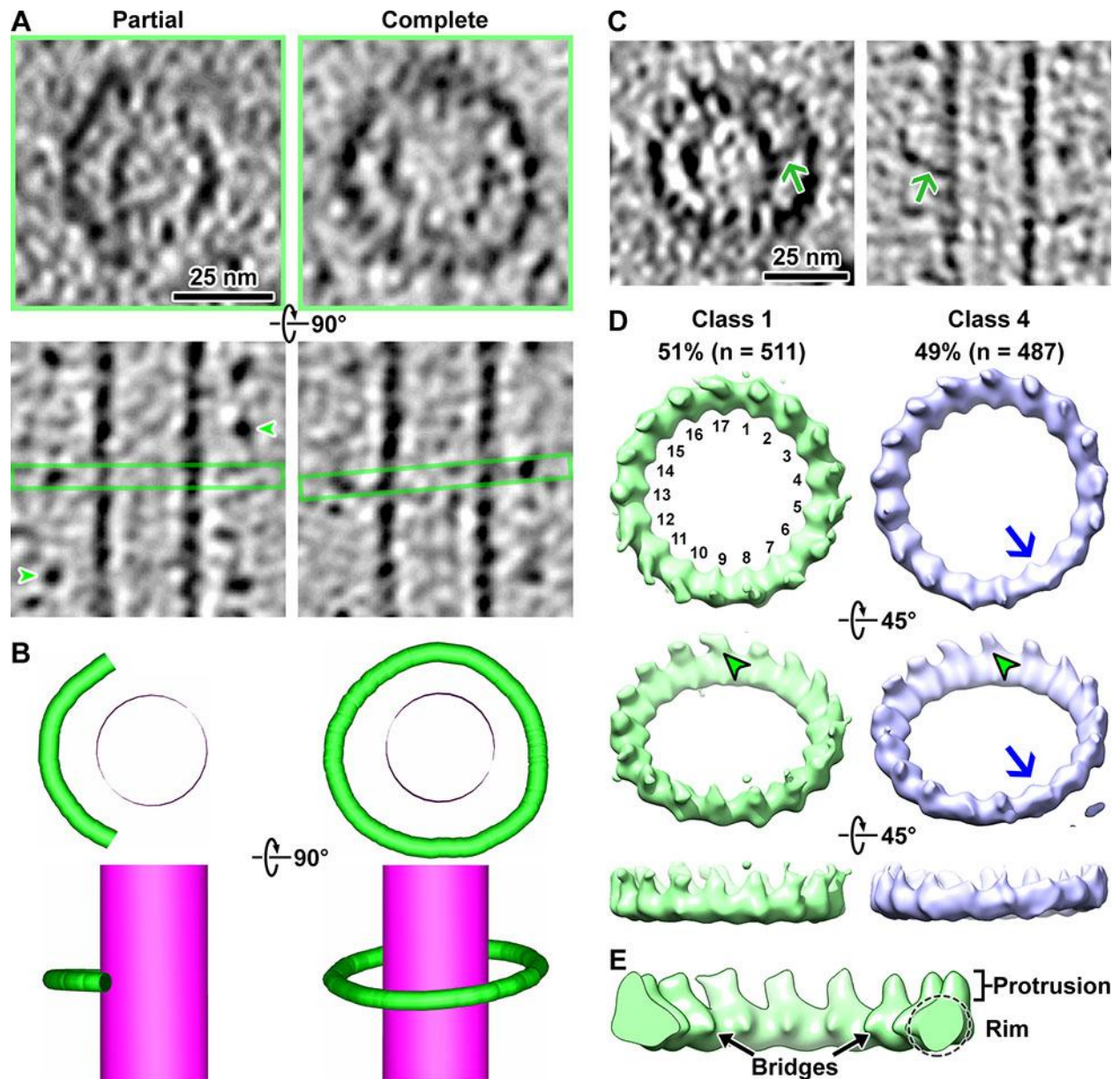
- 577 Abad, M.A., Medina, B., Santamaria, A., Zou, J., Plasberg-Hill, C., Madhumalar, A.,
578 Jayachandran, U., Redli, P.M., Rappsilber, J., Nigg, E.A., *et al.* (2014). Structural basis for
579 microtubule recognition by the human kinetochore Ska complex. *Nat Commun* 5, 2964.
- 580 Aravamudhan, P., Felzer-Kim, I., Gurunathan, K., and Joglekar, A.P. (2014). Assembling the
581 Protein Architecture of the Budding Yeast Kinetochore-Microtubule Attachment using FRET.
582 *Current biology* : CB 24, 1437-1446.
- 583 Asbury, C.L., Gestaut, D.R., Powers, A.F., Franck, A.D., and Davis, T.N. (2006). The Dam1
584 kinetochore complex harnesses microtubule dynamics to produce force and movement. *Proc*
585 *Natl Acad Sci USA* 103, 9873-9878.
- 586 Bharat, T.A., Russo, C.J., Lowe, J., Passmore, L.A., and Scheres, S.H. (2015). Advances in
587 Single-Particle Electron Cryomicroscopy Structure Determination applied to Sub-tomogram
588 Averaging. *Structure* 23, 1743-1753.
- 589 Bharat, T.A., and Scheres, S.H. (2016). Resolving macromolecular structures from electron
590 cryo-tomography data using subtomogram averaging in RELION. *Nat Protoc* 11, 2054-2065.
- 591 Caldas, G.V., and DeLuca, J.G. (2014). KNL1: bringing order to the kinetochore. *Chromosoma*
592 123, 169-181.
- 593 Cheeseman, I.M., Enquist-Newman, M., Müller-Reichert, T., Drubin, D.G., and Barnes, G.
594 (2001). Mitotic spindle integrity and kinetochore function linked by the Duo1p/Dam1p complex.
595 *The Journal of Cell Biology* 152, 197-212.
- 596 Chen, C., Lim, H.H., Shi, J., Tamura, S., Maeshima, K., Surana, U., and Gan, L. (2016).
597 Budding yeast chromatin is dispersed in a crowded nucleoplasm in vivo. *Mol Biol Cell* 27, 3357-
598 3368.
- 599 Dhatchinamoorthy, K., Shivaraju, M., Lange, J.J., Rubinstein, B., Unruh, J.R., Slaughter, B.D.,
600 and Gerton, J.L. (2017). Structural plasticity of the living kinetochore. *J Cell Biol.*
- 601 Dimitrova, Y.N., Jenni, S., Valverde, R., Khin, Y., and Harrison, S.C. (2016). Structure of the
602 MIND Complex Defines a Regulatory Focus for Yeast Kinetochore Assembly. *Cell* 167, 1014-
603 1027 e1012.
- 604 Efremov, A., Grishchuk, E.L., McIntosh, J.R., and Ataullakhanov, F.I. (2007). In search of an
605 optimal ring to couple microtubule depolymerization to processive chromosome motions.
606 *Proceedings of the National Academy of Sciences* 104, 19017-19022.
- 607 Franck, A.D., Powers, A.F., Gestaut, D.R., Gonen, T., Davis, T.N., and Asbury, C.L. (2007).
608 Tension applied through the Dam1 complex promotes microtubule elongation providing a direct
609 mechanism for length control in mitosis. *Nat Cell Biol* 9, 832-837.
- 610 Gan, L., Ladinsky, M.S., and Jensen, G.J. (2011). Organization of the smallest eukaryotic
611 spindle. *Curr Biol* 21, 1578-1583.

- 612 Gestaut, D.R., Graczyk, B., Cooper, J., Widlund, P.O., Zelter, A., Wordeman, L., Asbury, C.L.,
613 and Davis, T.N. (2008). Phosphoregulation and depolymerization-driven movement of the Dam1
614 complex do not require ring formation. *Nat Cell Biol* 10, 407-414.
- 615 Gillett, E.S., Espelin, C.W., and Sorger, P.K. (2004). Spindle checkpoint proteins and
616 chromosome-microtubule attachment in budding yeast. *J Cell Biol* 164, 535-546.
- 617 Gonen, S., Akiyoshi, B., Iadanza, M.G., Shi, D., Duggan, N., Biggins, S., and Gonen, T. (2012).
618 The structure of purified kinetochores reveals multiple microtubule-attachment sites. *Nat Struct*
619 *Mol Biol* 19, 925-929.
- 620 Goshima, G., and Yanagida, M. (2000). Establishing biorientation occurs with precocious
621 separation of the sister kinetochores, but not the arms, in the early spindle of budding yeast.
622 *Cell* 100, 619-633.
- 623 Hanisch, A., Silljé, H.H.W., and Nigg, E.A. (2006). Timely anaphase onset requires a novel
624 spindle and kinetochore complex comprising Ska1 and Ska2. *The EMBO Journal* 25, 5504-
625 5515.
- 626 Heumann, J.M. (2016). PEET (University of Colorado Boulder).
- 627 Heymann, J.B., and Belnap, D.M. (2007). Bsoft: image processing and molecular modeling for
628 electron microscopy. *J Struct Biol* 157, 3-18.
- 629 Hill, T.L. (1985). Theoretical problems related to the attachment of microtubules to kinetochores.
630 *Proc Natl Acad Sci U S A* 82, 4404-4408.
- 631 Hofmann, C., Cheeseman, I.M., Goode, B.L., McDonald, K.L., Barnes, G., and Drubin, D.G.
632 (1998). *Saccharomyces cerevisiae* Duo1p and Dam1p, novel proteins involved in mitotic spindle
633 function. *The Journal of Cell Biology* 143, 1029-1040.
- 634 Janczyk, P.Ł., Skorupka, K.A., Tooley, J.G., Matson, D.R., Kestner, C.A., West, T., Pomillos,
635 O., and Stukenberg, P.T. (2017). Mechanism of Ska Recruitment by Ndc80 Complexes to
636 Kinetochores. *Developmental Cell* 41, 438-449.e434.
- 637 Janke, C., Ortíz, J., Tanaka, T.U., Lechner, J., and Schiebel, E. (2002). Four new subunits of
638 the Dam1-Duo1 complex reveal novel functions in sister kinetochore biorientation. *EMBO J* 21,
639 181-193.
- 640 Jin, Q.W., Fuchs, J., and Loidl, J. (2000). Centromere clustering is a major determinant of yeast
641 interphase nuclear organization. *J Cell Sci* 113 (Pt 11), 1903-1912.
- 642 Joglekar, A.P., Bloom, K., and Salmon, E.D. (2009). In vivo protein architecture of the
643 eukaryotic kinetochore with nanometer scale accuracy. *Curr Biol* 19, 694-699.
- 644 Joglekar, A.P., Bouck, D., Finley, K., Liu, X., Wan, Y., Berman, J., He, X., Salmon, E.D., and
645 Bloom, K.S. (2008). Molecular architecture of the kinetochore-microtubule attachment site is
646 conserved between point and regional centromeres. *J Cell Biol* 181, 587-594.
- 647 Joglekar, A.P., and Kukreja, A.A. (2017). How Kinetochore Architecture Shapes the
648 Mechanisms of Its Function. *Curr Biol* 27, R816-R824.

- 649 Jones, M.H., Bachant, J.B., Castillo, A.R., Giddings, T.H., and Winey, M. (1999). Yeast Dam1p
650 is required to maintain spindle integrity during mitosis and interacts with the Mps1p kinase. *Mol*
651 *Biol Cell* *10*, 2377-2391.
- 652 Kimanius, D., Forsberg, B.O., Scheres, S.H., and Lindahl, E. (2016). Accelerated cryo-EM
653 structure determination with parallelisation using GPUs in RELION-2. *Elife* *5*.
- 654 Kitamura, E., Tanaka, K., Kitamura, Y., and Tanaka, T.U. (2007). Kinetochore microtubule
655 interaction during S phase in *Saccharomyces cerevisiae*. *Genes Dev* *21*, 3319-3330.
- 656 Kremer, J.R., Mastronarde, D.N., and McIntosh, J.R. (1996). Computer visualization of three-
657 dimensional image data using IMOD. *Journal of Structural Biology* *116*, 71-76.
- 658 Ladinsky, M.S. (2010). Micromanipulator-assisted vitreous cryosectioning and sample
659 preparation by high-pressure freezing. *Methods Enzymol* *481*, 165-194.
- 660 Lau, D.T., and Murray, A.W. (2012). Mad2 and Mad3 cooperate to arrest budding yeast in
661 mitosis. *Curr Biol* *22*, 180-190.
- 662 Legal, T., Zou, J., Sochaj, A., Rappsilber, J., and Welburn, J.P.I. (2016). Molecular architecture
663 of the Dam1 complex-microtubule interaction. *Open Biology* *6*.
- 664 Li, Y., Bachant, J., Alcasabas, A.A., Wang, Y., Qin, J., and Elledge, S.J. (2002). The mitotic
665 spindle is required for loading of the DASH complex onto the kinetochore. *Genes &*
666 *Development* *16*, 183-197.
- 667 Mastronarde, D.N. (1997). Dual-axis tomography: an approach with alignment methods that
668 preserve resolution. *Journal of Structural Biology* *120*, 343-352.
- 669 McEwen, B.F., Hsieh, C.E., Mattheyses, A.L., and Rieder, C.L. (1998). A new look at
670 kinetochore structure in vertebrate somatic cells using high-pressure freezing and freeze
671 substitution. *Chromosoma* *107*, 366-375.
- 672 McIntosh, J.R. (2005). Rings around kinetochore microtubules in yeast. *Nat Struct Mol Biol* *12*,
673 210-212.
- 674 McIntosh, J.R., O'Toole, E., Zhudenkov, K., Mophew, M., Schwartz, C., Ataulakhanov, F.I., and
675 Grishchuk, E.L. (2013). Conserved and divergent features of kinetochores and spindle
676 microtubule ends from five species. *J Cell Biol* *200*, 459-474.
- 677 Michaelis, C., Ciosk, R., and Nasmyth, K. (1997). Cohesins: chromosomal proteins that prevent
678 premature separation of sister chromatids. *Cell* *91*, 35-45.
- 679 Miranda, J.J., De Wulf, P., Sorger, P.K., and Harrison, S.C. (2005). The yeast DASH complex
680 forms closed rings on microtubules. *Nat Struct Mol Biol* *12*, 138-143.
- 681 Miranda, J.J., King, D.S., and Harrison, S.C. (2007). Protein arms in the kinetochore-
682 microtubule interface of the yeast DASH complex. *Mol Biol Cell* *18*, 2503-2510.
- 683 Mirchenko, L., and Uhlmann, F. (2010). Sli15(INCENP) dephosphorylation prevents mitotic
684 checkpoint reengagement due to loss of tension at anaphase onset. *Curr Biol* *20*, 1396-1401.

- 685 Murphy, G.E., Leadbetter, J.R., and Jensen, G.J. (2006). In situ structure of the complete
686 *Treponema primitia* flagellar motor. *Nature* 442, 1062-1064.
- 687 Musacchio, A., and Desai, A. (2017). A Molecular View of Kinetochore Assembly and Function.
688 *Biology (Basel)* 6.
- 689 Musacchio, A., and Salmon, E.D. (2007). The spindle-assembly checkpoint in space and time.
690 *Nat Rev Mol Cell Biol* 8, 379-393.
- 691 O'Toole, E.T., Mastronarde, D.N., Giddings, T.H., Jr., Winey, M., Burke, D.J., and McIntosh,
692 J.R. (1997). Three-dimensional analysis and ultrastructural design of mitotic spindles from the
693 *cdc20* mutant of *Saccharomyces cerevisiae*. *Mol Biol Cell* 8, 1-11.
- 694 Pettersen, E.F., Goddard, T.D., Huang, C.C., Couch, G.S., Greenblatt, D.M., Meng, E.C., and
695 Ferrin, T.E. (2004). UCSF Chimera--a visualization system for exploratory research and
696 analysis. *Journal of computational chemistry* 25, 1605-1612.
- 697 Ramey, V.H., Wong, A., Fang, J., Howes, S., Barnes, G., and Nogales, E. (2011). Subunit
698 organization in the Dam1 kinetochore complex and its ring around microtubules. *Mol Biol Cell*
699 22, 4335-4342.
- 700 Richmond, D., Rizkallah, R., Liang, F., Hurt, M.M., and Wang, Y. (2013). Slk19 clusters
701 kinetochores and facilitates chromosome bipolar attachment. *Mol Biol Cell* 24, 566-577.
- 702 Tachiwana, H., Kagawa, W., Shiga, T., Osakabe, A., Miya, Y., Saito, K., Hayashi-Takanaka, Y.,
703 Oda, T., Sato, M., Park, S.Y., *et al.* (2011). Crystal structure of the human centromeric
704 nucleosome containing CENP-A. *Nature* 476, 232-235.
- 705 Tanaka, K., Kitamura, E., Kitamura, Y., and Tanaka, T.U. (2007). Molecular mechanisms of
706 microtubule-dependent kinetochore transport toward spindle poles. *The Journal of Cell Biology*
707 178, 269-281.
- 708 Tanaka, K., Mukae, N., Dewar, H., van Breugel, M., James, E.K., Prescott, A.R., Antony, C.,
709 and Tanaka, T.U. (2005). Molecular mechanisms of kinetochore capture by spindle
710 microtubules. *Nature* 434, 987-994.
- 711 Tanaka, T.U. (2010). Kinetochore-microtubule interactions: steps towards bi-orientation. *EMBO*
712 *J* 29, 4070-4082.
- 713 Tang, G., Peng, L., Baldwin, P.R., Mann, D.S., Jiang, W., Rees, I., and Ludtke, S.J. (2007).
714 EMAN2: an extensible image processing suite for electron microscopy. *J Struct Biol* 157, 38-46.
- 715 Uhlmann, F., Wernic, D., Poupart, M.A., Koonin, E.V., and Nasmyth, K. (2000). Cleavage of
716 cohesin by the CD clan protease separin triggers anaphase in yeast. *Cell* 103, 375-386.
- 717 van Hooff, J.J.E., Snel, B., and Kops, G.J.P.L. (2017). Unique Phylogenetic Distributions of the
718 Ska and Dam1 Complexes Support Functional Analogy and Suggest Multiple Parallel
719 Displacements of Ska by Dam1. *Genome biology and evolution* 9, 1295-1303.
- 720 Wang, H.-W., Ramey, V.H., Westermann, S., Leschziner, A.E., Welburn, J.P.I., Nakajima, Y.,
721 Drubin, D.G., Barnes, G., and Nogales, E. (2007). Architecture of the Dam1 kinetochore ring

- 722 complex and implications for microtubule-driven assembly and force-coupling mechanisms. *Nat*
723 *Struct Mol Biol* *14*, 721-726.
- 724 Wang, H.W., Long, S., Ciferri, C., Westermann, S., Drubin, D., Barnes, G., and Nogales, E.
725 (2008). Architecture and flexibility of the yeast Ndc80 kinetochore complex. *J Mol Biol* *383*, 894-
726 903.
- 727 Welburn, J.P.I., Grishchuk, E.L., Backer, C.B., Wilson-Kubalek, E.M., Yates, J.R., and
728 Cheeseman, I.M. (2009). The human kinetochore Ska1 complex facilitates microtubule
729 depolymerization-coupled motility. *Developmental Cell* *16*, 374-385.
- 730 Westermann, S., Avila-Sakar, A., Wang, H.-W., Niederstrasser, H., Wong, J., Drubin, D.G.,
731 Nogales, E., and Barnes, G. (2005). Formation of a dynamic kinetochore- microtubule interface
732 through assembly of the Dam1 ring complex. *Molecular Cell* *17*, 277-290.
- 733 Westermann, S., Wang, H.-W., Avila-Sakar, A., Drubin, D.G., Nogales, E., and Barnes, G.
734 (2006). The Dam1 kinetochore ring complex moves processively on depolymerizing microtubule
735 ends. *Nature* *440*, 565-569.
- 736 Winey, M., Mamay, C.L., O'Toole, E.T., Mastronarde, D.N., Giddings, T.H., Jr., McDonald, K.L.,
737 and McIntosh, J.R. (1995). Three-dimensional ultrastructural analysis of the *Saccharomyces*
738 *cerevisiae* mitotic spindle. *J Cell Biol* *129*, 1601-1615.
- 739 Xiong, Q., Morphew, M.K., Schwartz, C.L., Hoenger, A.H., and Mastronarde, D.N. (2009). CTF
740 determination and correction for low dose tomographic tilt series. *Journal of Structural Biology*
741 *168*, 378-387.
- 742 Yakovlev, S., and Downing, K.H. (2011). Freezing in sealed capillaries for preparation of frozen
743 hydrated sections. *J Microsc* *244*, 235-247.
- 744 Zelter, A., Bonomi, M., Kim, J.o., Umbreit, N.T., Hoopmann, M.R., Johnson, R., Riffle, M.,
745 Jaschob, D., MacCoss, M.J., Moritz, R.L., *et al.* (2015). The molecular architecture of the Dam1
746 kinetochore complex is defined by cross-linking based structural modelling. *Nature*
747 *Communications* *6*, 8673.
- 748 Zhang, Q., Sivakumar, S., Chen, Y., Gao, H., Yang, L., Yuan, Z., Yu, H., and Liu, H. (2017).
749 Ska3 Phosphorylated by Cdk1 Binds Ndc80 and Recruits Ska to Kinetochores to Promote
750 Mitotic Progression. *Current biology : CB* *27*, 1477-1484.e1474.
751

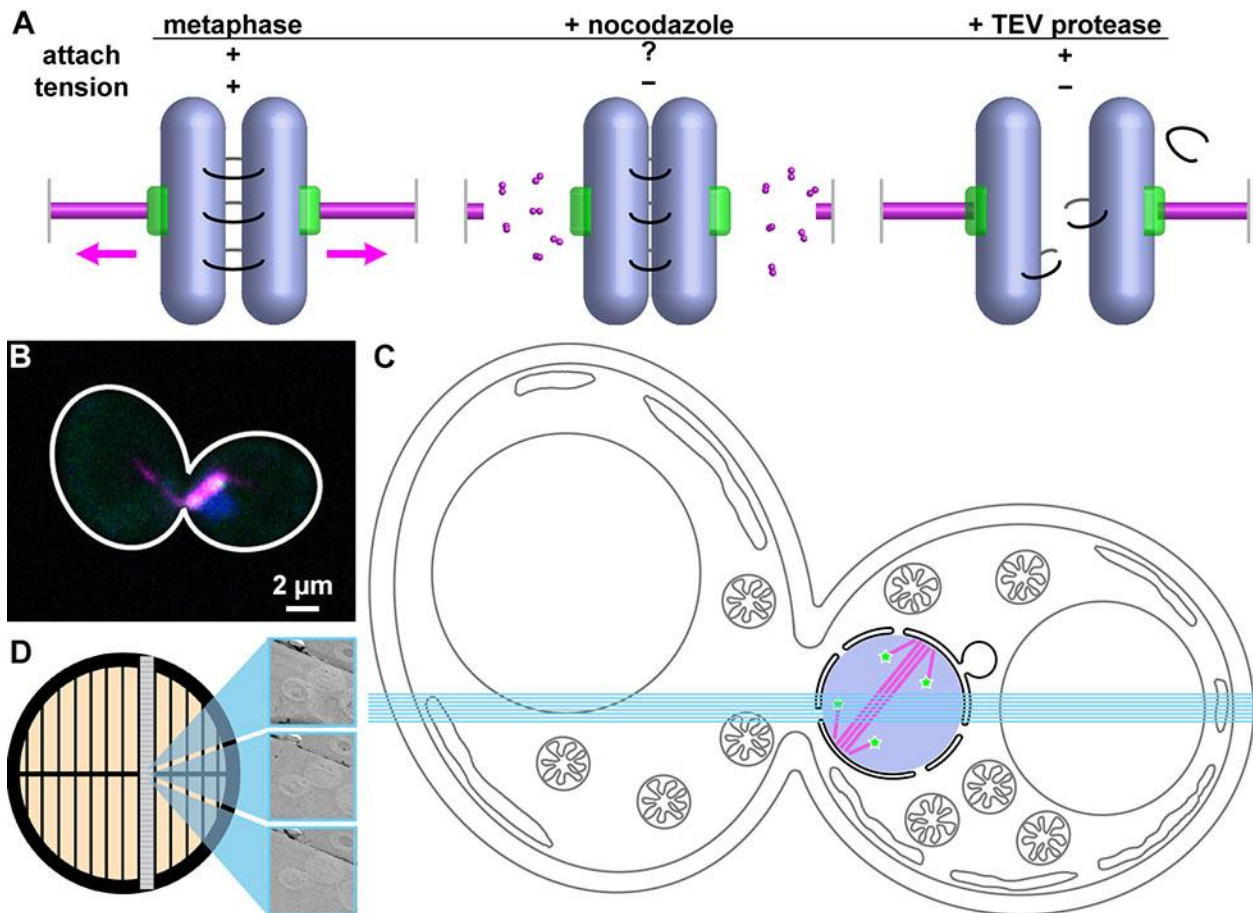


752

753 **Figure 1. Dam1C/DASH oligomerizes into partial and complete rings *in vitro***

754 (A) Cryotomographic slices (4.6 nm) showing front views of partial (left) and complete
 755 (right) Dam1C/DASH rings assembled around MTs. The lower row shows the same
 756 rings but rotated 90° around the horizontal axis. Green arrowheads: densities of
 757 adjacent Dam1C/DASH oligomers; green rectangles: approximate planes of the partial
 758 or complete ring taken in the upper panels. (B) Three-dimensional models of
 759 Dam1C/DASH and MT complexes corresponding to upper and lower rows in panel A.

760 (C) Two examples of Dam1C/DASH rings with bridges (green arrows), in the front (left)
761 and side (right) views. (D) Asymmetric 3-D class averages of Dam1C/DASH rings
762 around MTs. Repeat subunits are numbered for class 1. Classes 2 and 3 (not shown)
763 are very similar to class 4 and were included in the 49%. The upper image is the front
764 view. The middle and lower panels are sequentially rotated 45° around the horizontal
765 axis. Green arrowheads: protrusions. Blue arrow: position in class average 4 that
766 deviates from 17-fold symmetry. All density maps were masked to exclude the MT and
767 contoured at 0.1 σ above the mean. (E) Enlarged, cutaway view of a 17-fold
768 symmetrized Dam1C/DASH ring, with landmark motifs labeled. Note that the bridges
769 appear shorter than in the individual subtomograms because their structures are
770 extremely heterogeneous.

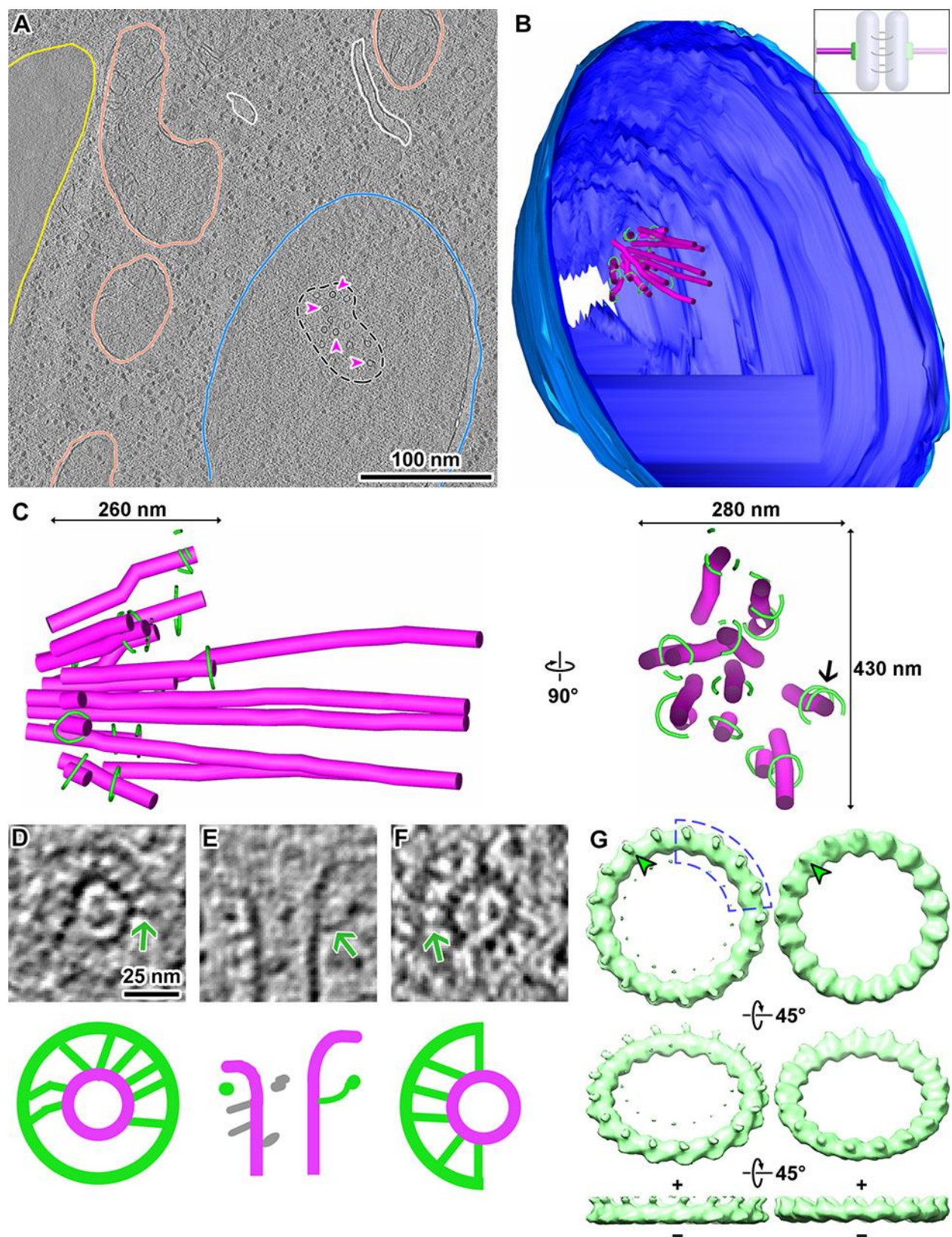


771

772 **Figure 2. Strategy to find kinetochores *in vivo***

773 (A) Schematic of kinetochore states studied in this paper, not to scale. Sister
774 chromosomes (pale-blue rods) are held under tension (magenta arrows) in metaphase
775 when kMT (magenta tubes) pulling forces are transmitted by cohesin (curved lines).
776 Gray vertical bars: spindle-pole bodies. Tension at the kinetochores (green) can be
777 eliminated either by the disruption of the kMTs with nocodazole or the conditional
778 cleavage of mutant cohesin with TEV protease. This color scheme is used throughout
779 the paper. (B) Immunofluorescence image of a Cdc20-depleted cell, with Dam1p-GFP
780 in green and Tubulin in magenta. Owing to the merged channels, Dam1C/DASH
781 appears white. (C) Cartoon of a mitotic yeast cell, with organelles drawn to approximate
782 scale. The nucleus (pale blue circle), spindle (magenta lines), and kinetochores (green

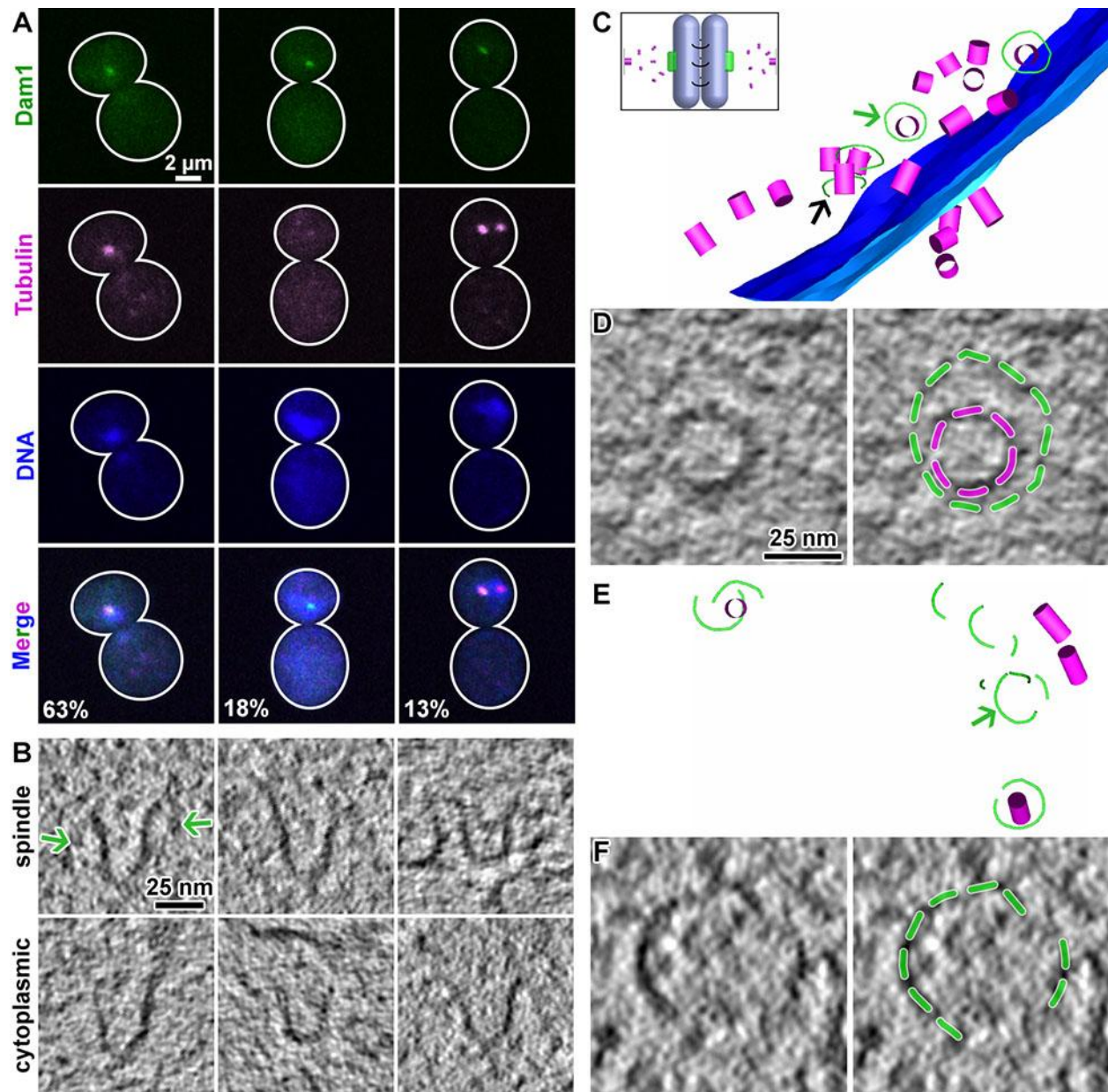
783 stars, not to scale) are colored. Cyan lines illustrate at scale a series of seven ~ 100-nm
784 cryosections. (D) Serial cryotomography strategy. Cryo-EM images of sequential
785 cryosections of the same cell mounted on a parallel-bar grid are shown enlarged ~ 100-
786 fold on the right.



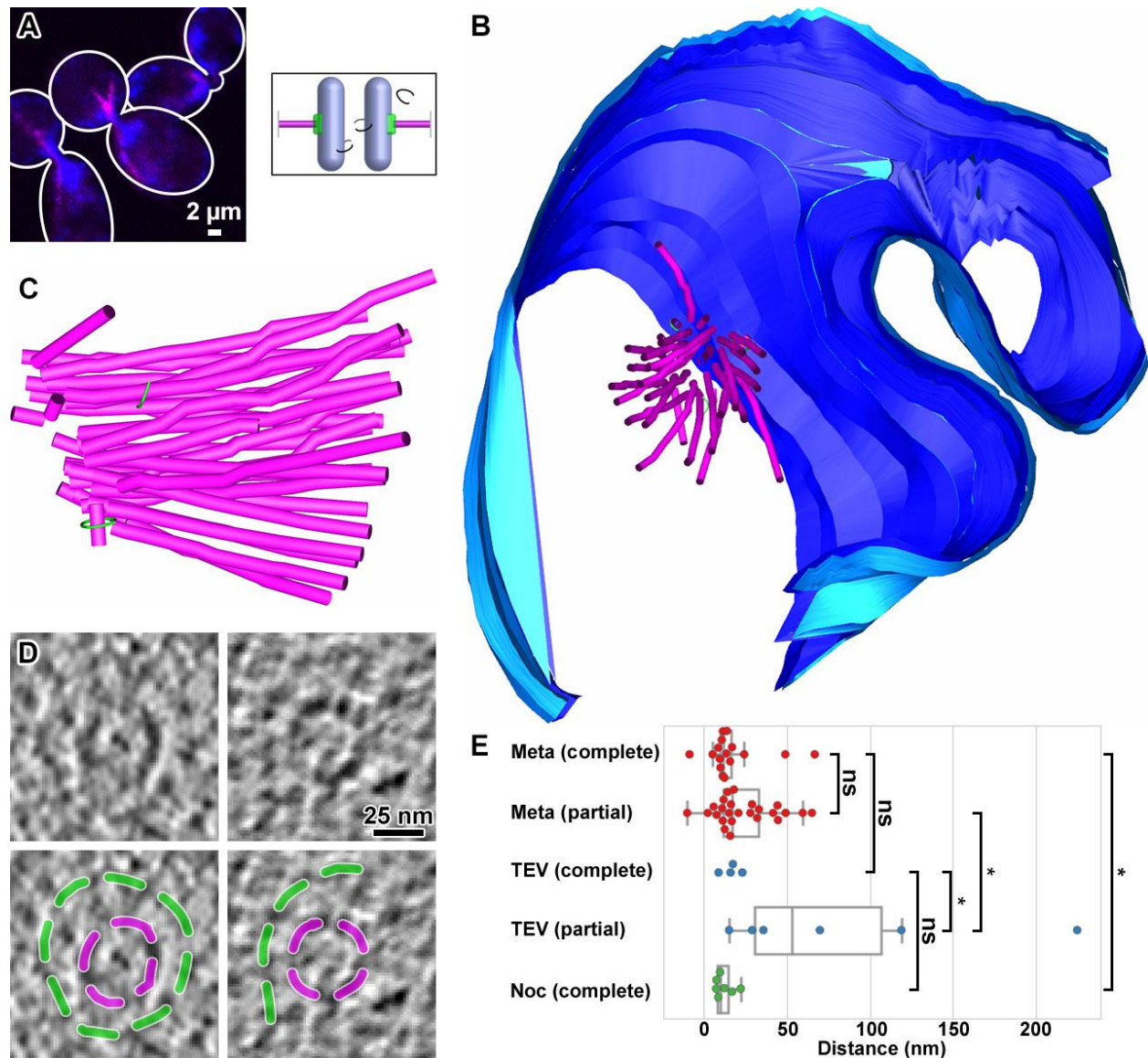
787

788 **Figure 3. Architecture of metaphase spindles and outer kinetochores**

789 (A) Cryotomographic slice (18 nm) from a Cdc20-depleted cell. Major features are
790 annotated: cell membrane (yellow), mitochondria (salmon), endoplasmic reticulum
791 (white), nucleus (blue). The black dashes outline the spindle. A few spindle MTs are
792 indicated with magenta arrowheads. (B) Three-dimensional model of a half spindle,
793 spanning 7 sequential sections. Dark and light blue: inner and outer nuclear
794 membranes. Magenta tubes: spindle MTs. Green rings: Dam1C/DASH. Inset: schematic
795 showing the structures that are modeled (saturated shading) and those that are not
796 (washed-out shading). (C) Left: Enlargement of the spindle modeled in panel B and
797 rotated to a view perpendicular to the spindle's axis. Right: Transverse view of the same
798 spindle; for clarity, polar MTs are omitted. Because the short axis crosses multiple
799 cryosection interfaces, we are uncertain how long this spindle was in the unsectioned
800 cell. This particular spindle also has an oval cross section due to microtomy
801 compression along the X axis of the right panel. Black arrow: one example of a kMT
802 with two partial rings. (D - F) Cryotomographic slices (6 nm) of Dam1C/DASH rings
803 around kMTs. Green arrows point to bridges. The lower panels show schematics of the
804 Dam1C/DASH (green), kMT (magenta), and kMT-associated protein (gray) densities.
805 Panels D and F show front views of a complete and partial ring, respectively. Panel E
806 shows a side view of a complete ring. (G) Rotationally averaged density maps of two
807 individual complete Dam1C/DASH rings *in vivo*, masked to exclude the kMT, contoured
808 at 1σ above the mean. Top: front view. The middle and lower rows are sequentially
809 rotated 45° around the horizontal axis. Green arrowheads: protrusions. The plus and
810 minus signs indicate the polarity of the encircled kMT. If four or more decamers
811 (outlined by blue dashes) were absent, there would be a gap > 25 nm.



819 nocodazole-disrupted spindle with complete Dam1C/DASH rings associated with short
820 MTs. Part of the bottom-most Dam1C/DASH ring (black arrow) could not be modeled
821 because it was located near the cryosection's surface. Green arrow: Dam1C/DASH ring
822 that is enlarged in panel D. Inset: schematic showing the effect of nocodazole
823 treatment. (D) Left: cryotomographic slice (8 nm) showing the front view of a complete
824 Dam1C/DASH ring on a short kMT. Right: the same cryotomographic slice but
825 annotated with green dashes over the Dam1C/DASH densities and magenta dashes
826 over the MT densities. (E) Model of unattached Dam1C/DASH oligomers and MT
827 fragments in the nucleoplasm. Green arrow: partial Dam1C/DASH ring that is enlarged
828 in panel F. (F) Left: cryotomographic slice (8 nm) showing unattached Dam1C/DASH
829 partial rings. Right: the same cryotomographic slice but annotated with green dashes
830 overlaying the Dam1C/DASH densities.



831

832 **Figure 5. Architecture of spindle machinery in mitotic cells without cohesion**

833 (A) Immunofluorescence image of a metaphase-arrested cell (Cdc20 depleted) in which

834 tension is absent because the cohesin subunit Scc1 is cleaved by TEV protease. Blue:

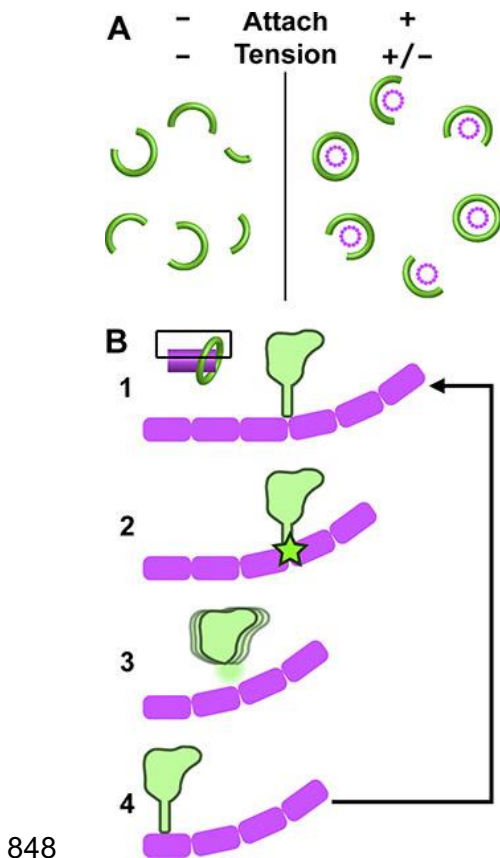
835 DNA. Magenta: MTs. Inset: schematic showing the loss of cohesion. (B) Serial cryo-ET

836 model of one such cell. The nuclear envelope is colored blue and the spindle MTs

837 colored magenta. The few Dam1C/DASH rings that were found are colored green. Note

838 that the discontinuities in the nuclear envelope model are from the interfaces between

839 adjacent cryosections, which could not be accurately modeled. (C) Enlargement of the
840 spindle modeled in panel B, rotated to a view perpendicular to the spindle's axis. (D)
841 Cryotomographic slices (6 nm) of front views of complete (left) and partial (right)
842 Dam1C/DASH rings around kMTs. (E) Box-and-whisker plots and raw values (colored
843 circles) of the distances between kMT plus ends and Dam1C/DASH ring centers of
844 mass. Two Dam1C/DASH rings were located in front of kMT plus ends, which gave rise
845 to negative distance values. Meta: cells arrested in metaphase. TEV: cells arrested in
846 metaphase and with Scc1 cleaved. Noc: cells treated with nocodazole. ns: not
847 significant, Student's t-test $p > 0.05$. Asterisk: F-test of equal variance $p < 0.01$.



848

849 **Figure 6. A multi-scale model of the yeast mitotic machinery *in vivo***

850 (A) Cartoon of clusters of Dam1C/DASH rings, viewed along the spindle axis.

851 Dam1C/DASH (green) can only form complete rings when attached to kMTs (magenta).

852 (B) Inset: cartoon of a single Dam1C/DASH-kinetochore attachment site. The boxed

853 area is enlarged, showing a schematic of Dam1C/DASH in cross section (green) and

854 tubulin dimers (magenta rounded rectangles). (1) The bridge is stably engaged with the

855 flat surface of an MT until (2) the peeling protofilament becomes locally curved enough

856 to destabilize the bridge's interaction. (3) If enough Dam1C/DASH bridges are freed, the

857 ring can diffuse along the kMT axis until it encounters a flat portion of the MT. (4) Here

858 the bridge makes a stable contact again, attaching Dam1C/DASH to a position closer to

859 the minus end.

860

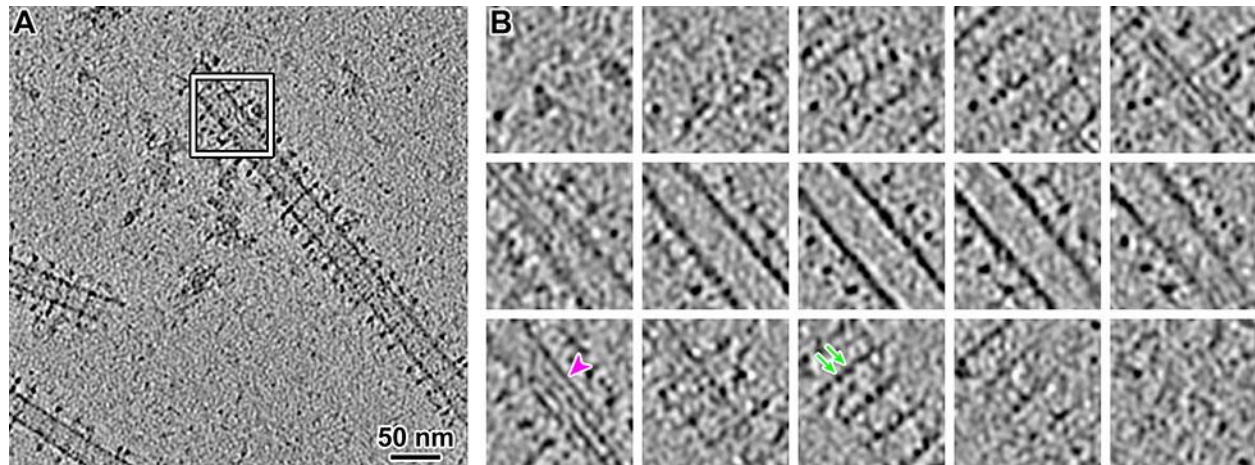
Supplemental Information

861

862 **A multi-scale model of the yeast chromosome-segregation system**

863

864 Cai Tong Ng, Li Deng, Chen Chen, Hong Hwa Lim, Jian Shi, Uttam Surana, and Lu Gan



865

866 **Figure S1. Example plunge-frozen MTs with Dam1C/DASH rings**

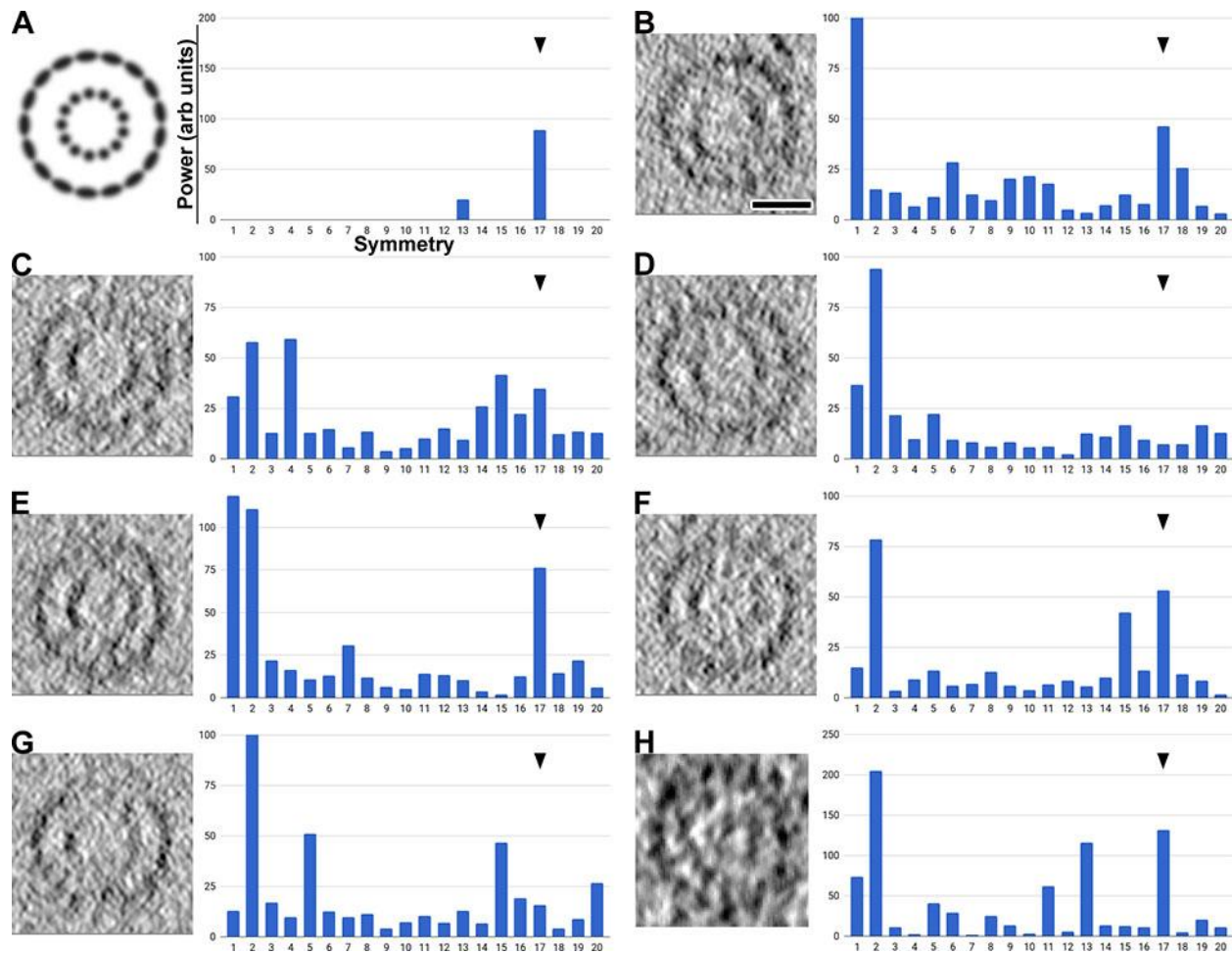
867 (A) Cryotomographic slice (60 nm) of MTs, encircled by Dam1C/DASH rings. The

868 amorphous densities below and to the left of the white box are protein aggregates. (B) A

869 series of cryotomographic slices (5 nm) through the position boxed in white in panel A,

870 enlarged twofold. The magenta arrowhead and green arrows indicate a MT

871 protofilament and Dam1C/DASH decamers, respectively.



872

873 **Figure S2. Rotational symmetry analysis of Dam1C/DASH rings *in vivo* and *in***

874 ***vitro***

875 (A) Left: Manually constructed image with perfect 17-fold (outer) and 13-fold (inner)

876 symmetries. The radii of the outer and inner arrays and their aspect ratios are to the

877 approximate scales of a front view of Dam1C/DASH around MTs. Right: Rotational

878 power spectrum of the densities on the left. The Y axis is the power (arbitrary units) and

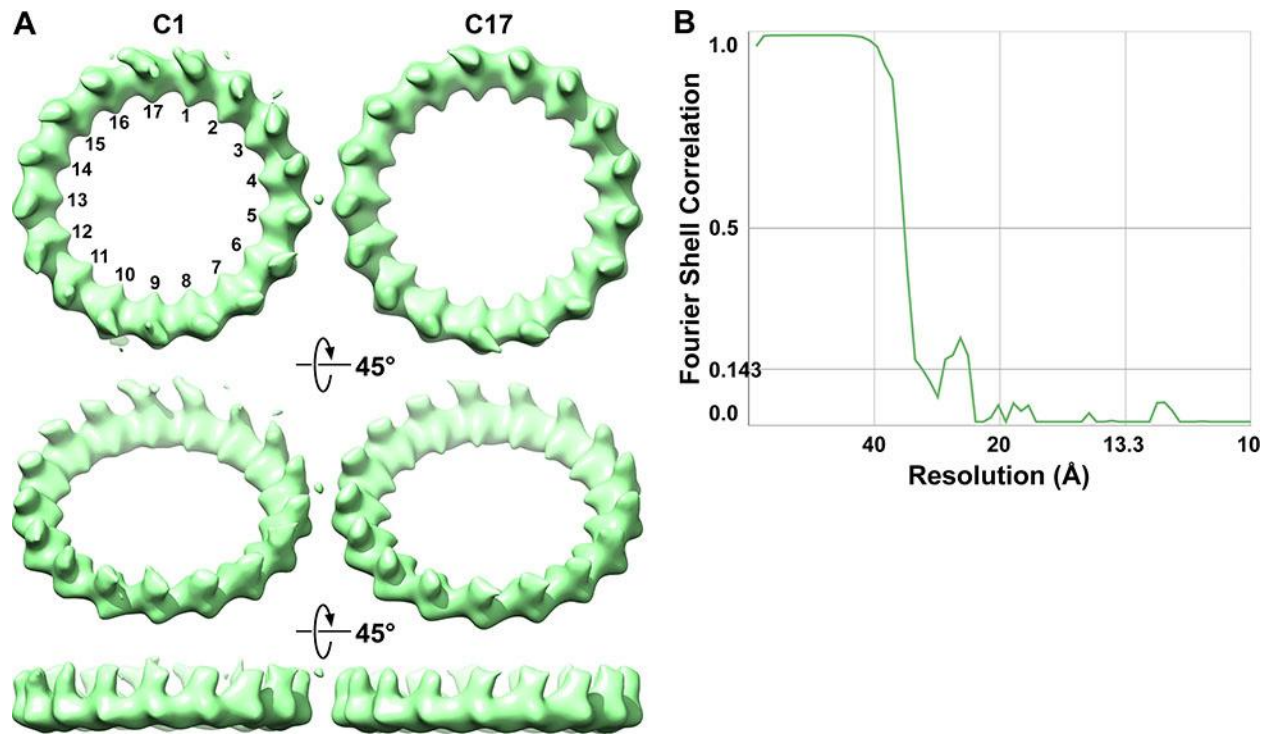
879 the X axis is the rotational symmetry. Seventeen-fold symmetry is indicated by the black

880 arrowhead. All subsequent plots have the same axes. (B - G) Left: Cryotomographic

881 slices of Dam1C/DASH ring around MTs *in vitro*, rotated to the front view. Right: Power

882 spectra of the cryotomographic slices. Bar = 25 nm for all cryotomographic slices. The

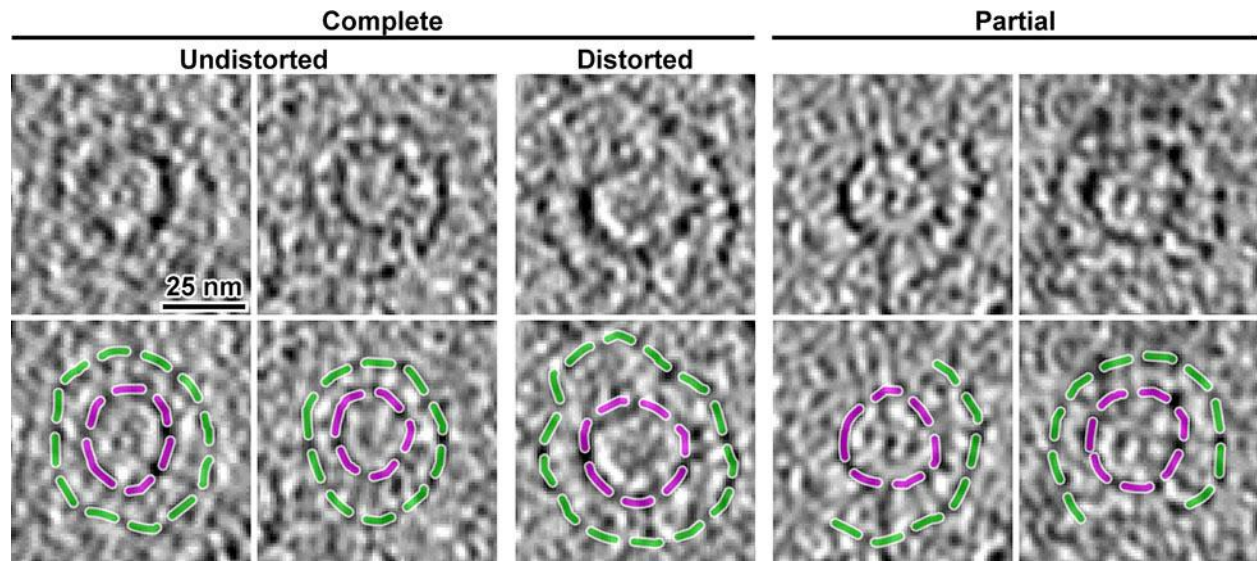
883 non-Dam1C/DASH densities were masked prior to power spectrum analysis, but the
884 mask is not shown. Some rings, such as that in panels D and G, are distorted and do
885 not produce a strong peak. The 15-fold symmetry peak comes from the MT densities
886 (many MTs have 15-protofilaments *in vitro*), which can leak out of the mask due to the
887 missing-wedge. Note that because these cryotomographic slices were taken coplanar
888 with the Dam1C/DASH ring, the symmetry signal from the MTs are weak or absent
889 when the ring is tilted. (H) Left: cryotomographic slice (6 nm) showing the front view of a
890 Dam1C/DASH ring around a MT *in vivo*. Right: Rotational power spectrum.



891

892 **Figure S3. Three-dimensional rotational symmetry analysis of Dam1C/DASH *in***
893 ***vitro***

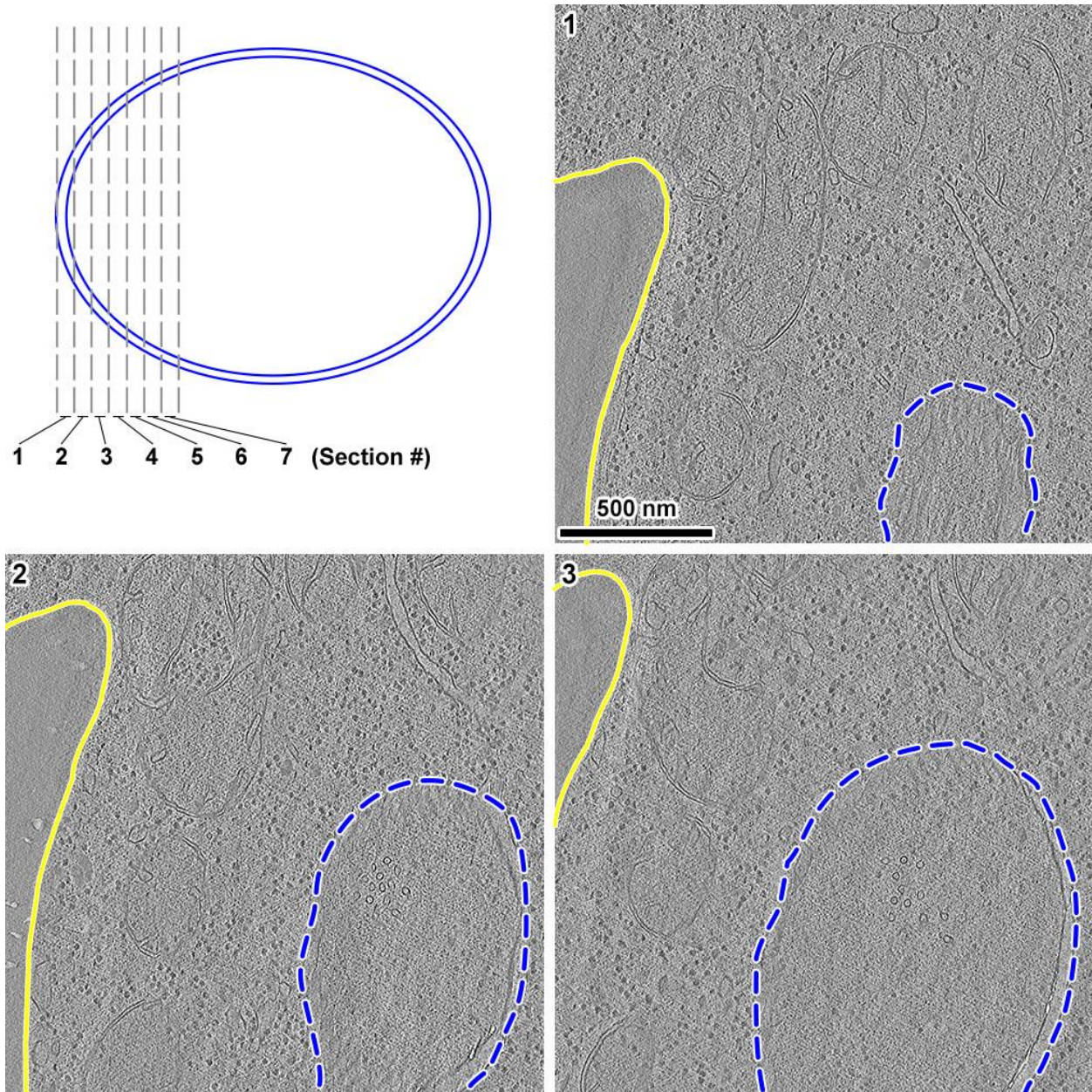
894 (A) Subtomogram averages of Dam1C/DASH rings around MTs, without (C1) or with
895 17-fold (C17) symmetry imposed. The unsymmetrized densities (C1) and subunit
896 numbering are reproduced from Fig. 1D. Only the most symmetric complexes,
897 corresponding to those that resemble Class 1 in Fig. 1, were symmetrized. The upper
898 row is the front view. Each row below is sequentially rotated 45° around the horizontal
899 axis. (B) On the basis of the Fourier-shell correlation = 0.143 criterion, the resolution of
900 the 17-fold symmetrized reconstruction is 32 Å.



901

902 **Figure S4. Dam1C/DASH rings can be visualized in cryosections**

903 Dam1C/DASH rings and MTs were assembled *in vitro*, high-pressure frozen, and then
904 cryosectioned. Upper row: cryotomographic slices (6 nm) of Dam1C/DASH rings around
905 MTs. Lower row: dashed lines corresponding to Dam1C/DASH (green) and MT
906 (magenta) densities have been superposed on a copy of the upper panel.



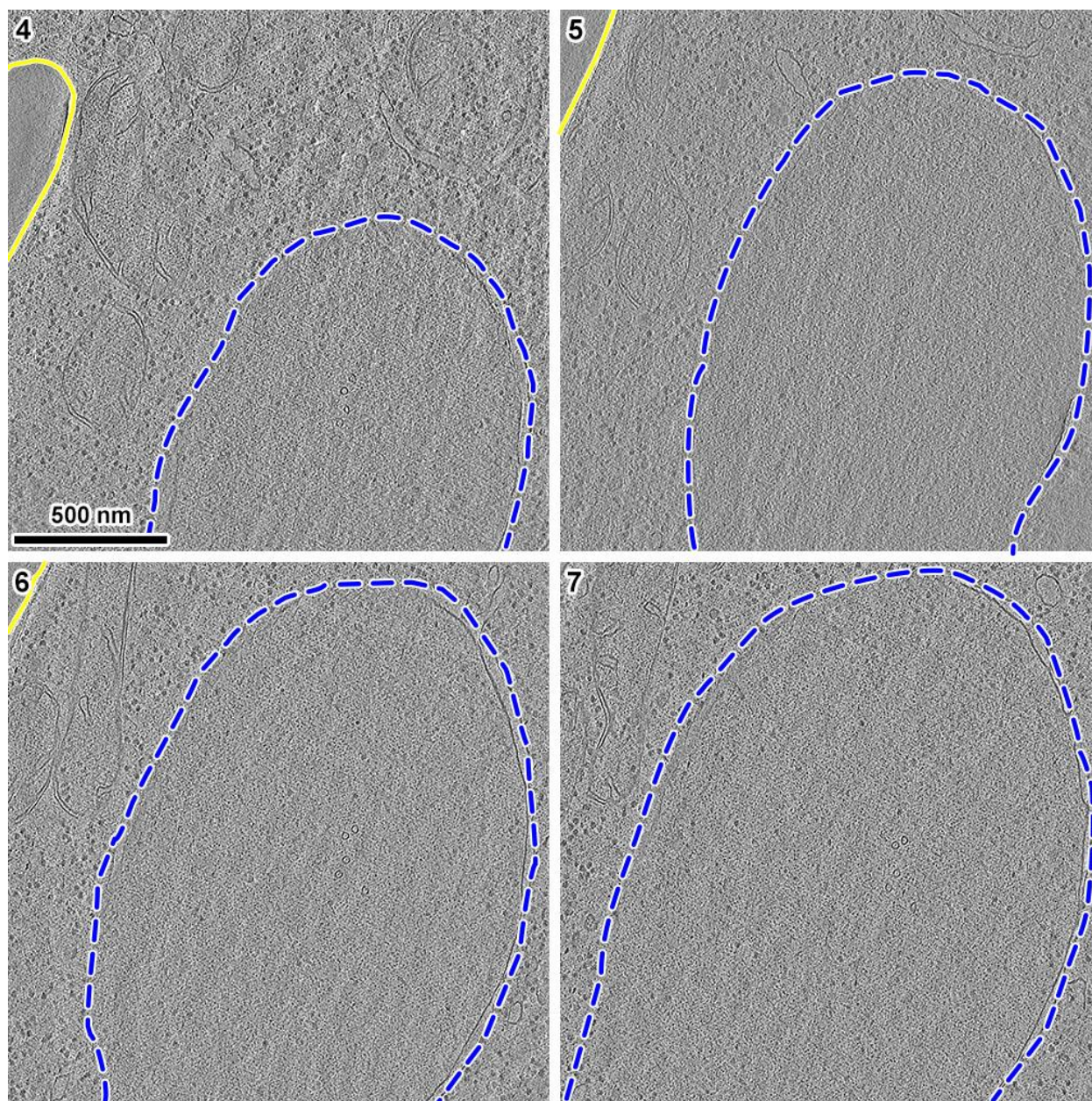
907

908 **Figure S5, part 1. Serial cryotomograms 1 - 3 of a metaphase yeast cell.**

909 (Upper left panel) Cartoon of a cell nucleus, bounded by a nuclear envelope (double
910 blue lines). Seven sequential sections are shown, bordered by vertical gray dashes.

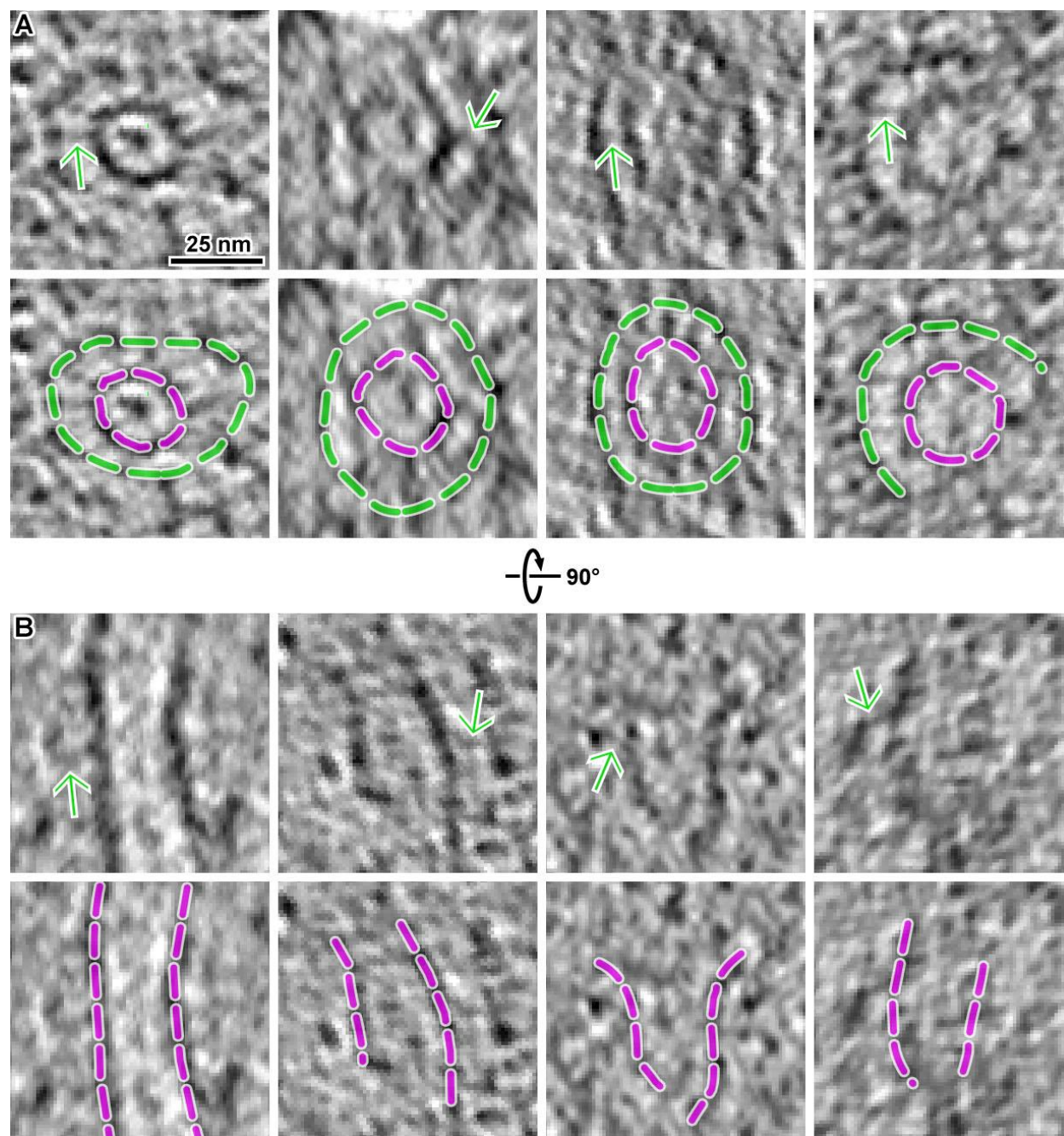
911 Sections are numbered at the upper left of each panel. (Panels 1 - 3) Cryotomographic
912 slices (20 nm) of 3 sequential cryosections of a metaphase cell. The outer nuclear

913 membrane is outlined in blue dashes in each panel. The plasma membrane is outlined
914 by a solid yellow line.



915

916 **Figure S5, part 2. Serial cryotomograms 4 - 7 of a metaphase yeast cell.**

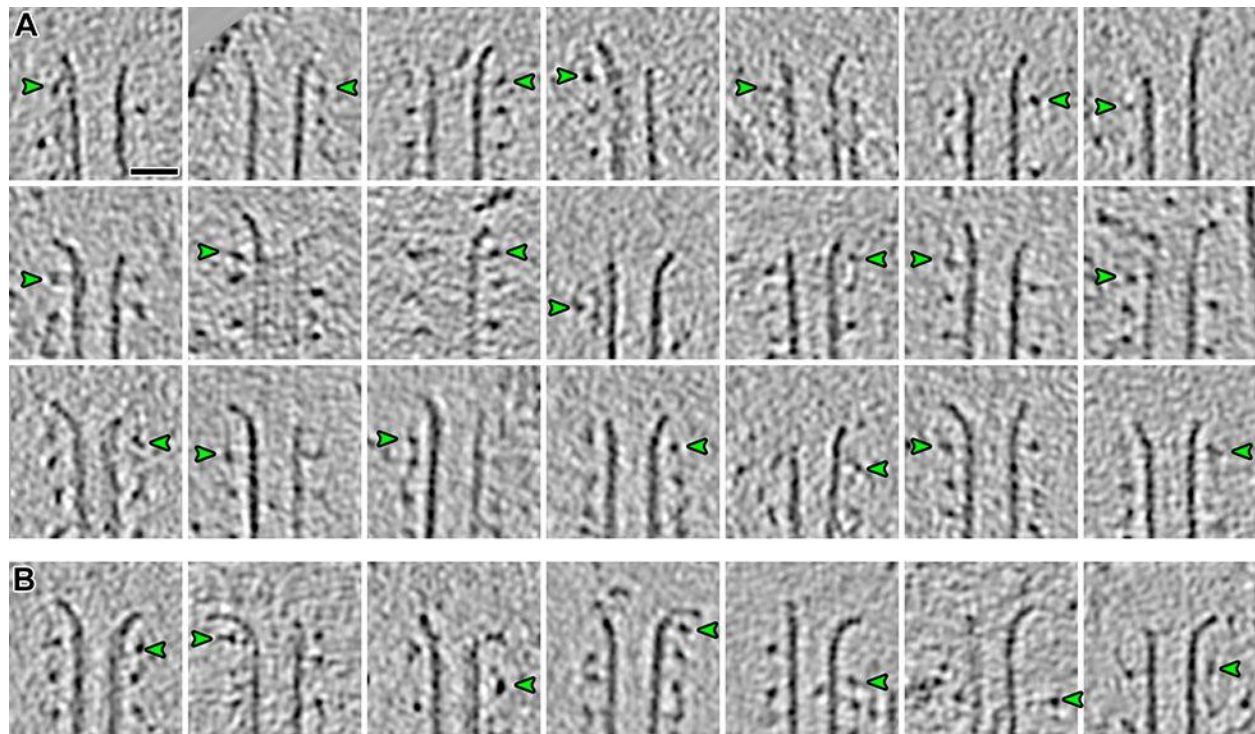


917

918 **Figure S6. Dam1C/DASH bridges are conformationally heterogeneous *in vivo***

919 (A) Cryotomographic slices (5 nm) showing four examples of bridges (green arrows) on
920 both complete and partial Dam1C/DASH rings (green dashes) attached to kMT walls
921 (magenta dashes) in metaphase cells. For clarity, the upper and lower panels show the

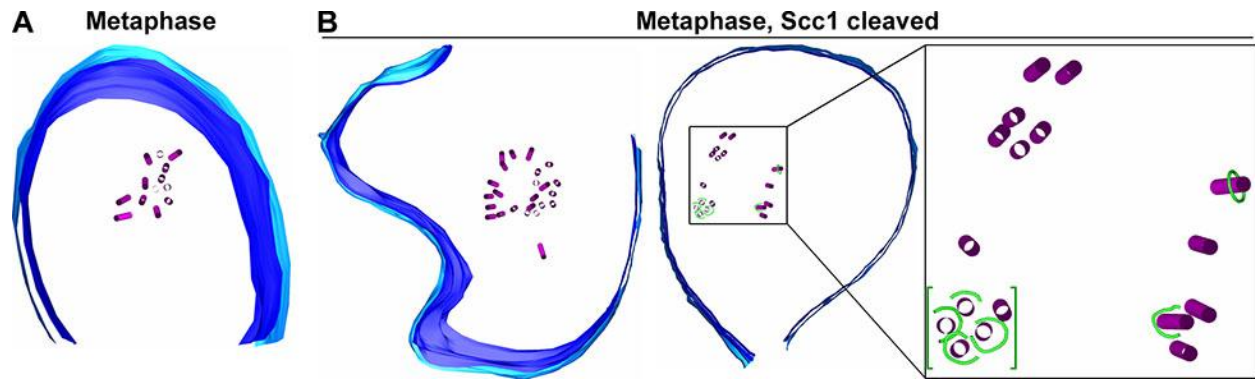
- 922 same densities but with different sets of annotations. (B) Same structures as in panel A
- 923 but rotated 90° around the horizontal axis.



924

925 **Figure S7. Curved protofilaments rarely contact Dam1C/DASH *in vitro***

926 (A) Cryotomographic slices (4.6 nm) of the flared ends of MTs assembled with
927 Dam1C/DASH *in vitro*. Green arrowheads indicate the Dam1C/DASH density closest to
928 protofilaments' curved tip. Scale bar, 25 nm. (B) Same as in panel A but for MTs
929 showing the ram's horn tip motifs. Note that some MTs appear narrower than 25 nm in a
930 subset of slices taken closer to the surface of the MT. Another subset of MTs have
931 lower contrast because they were oriented almost perpendicular to the tilt axis; this is a
932 well-known missing-wedge effect that changes the appearance of tubular structures.



933

934 **Figure S8. Loss of tension changes the spindle shape and kinetochore**
935 **distribution**

936 (A) A model of a portion of a metaphase spindle. MTs are magenta and the nuclear

937 envelope membranes are blue. (B) Models of two metaphase spindles with Scc1

938 cleaved. These models came from single cryosections that were cut almost exactly

939 transverse to the spindle axis. In metaphase cells without tension (Scc1 cleaved), the

940 spindle MTs are arranged in isolated bundles surrounding a MT-free core. The spindle

941 on the right (boxed) includes Dam1C/DASH rings (green) and is enlarged 3.5-fold on

942 the right inset. Note that Dam1C/DASH rings within the cluster (green brackets) were

943 spread out along spindle axis (coming out of the image) and were not in contact.

944 **Table S1. Summary of observations**

Condition	Spindle	Attach	Tension	SAC	Dam1C/DASH rings			kMT
					Complete	Partial	n	nm
Metaphase	Intact	+	+	OFF	39%	61%	46	50 - 200+
Nocodazole treatment	MT stubs	+	-	ON	86%	14%	7	20 - 50
	absent	-	-	ON	0%	100%	37	n/a
Metaphase, Scc1 cleaved	Distorted	+	-	ON	39%	61%	33	50 - 200+

945

946 n/a: kMT length unknown because they were not within the same cryosection as the

947 kinetochore. Note that out of 86 attached Dam1C/DASH rings, kMT-tip-to-

948 Dam1C/DASH distances could be measured for only 56 of them.

949 **Table S2.** Strains used for this study

Strain	Genotype	Origin	Experiment
US1375	MATa ura3 cdc20D: LEU2 his3 GAL-CDC20::TRP1	Liang, 2012	Metaphase arrest
US1363	MATa bar1 Δ ade2-1 can1-100 leu2-3 his3-11 ura3 trp1-1 (Wild type)	Krishnan, 2004	Nocodazole treatment
US8133	MATa bar1-1, ura3-1, leu2-3,112, his3-11, can1-100, ade2-1 <i>Dam1-GFP:TRP1</i>	This study	
US4780	MATa, MET3-HA-CDC20: URA3, scc1D: HIS3, SCC1TEV268-HA3-LEU2, GAL-NLS-myc9-TEV protease-NLS2::TRP1, tetR-GFP: HIS3	This study	Metaphase arrest, Scc1 cleaved

950

951 **Table S3. Imaging parameters**

Sample	<i>S. cerevisiae</i> cells	Dam1C/DASH + MT, cryosections	Dam1C/DASH + MT, plunge frozen
Grid type	CF-42-2C-T; continuous carbon	CF-22-2C-T (Protochips)	Quantifoil R2/2
Microscope		Titan Krios	
Voltage		300 kV	
Gun type		FEG	
Camera		Falcon II Direct Detector	
Software		TOMO4	
Calibrated magnification	15,678 / 19,167	30,369	30,369
Calibrated pixel	8.93 / 7.3 Å	4.61 Å	4.61 Å
Defocus	-8 to -15 µm Volta: -0.5 µm	-10 µm	-8 to -14 µm Volta: -0.5 µm
Cumulative dose		100 - 130 e/Å ²	
Dose fractionation		1 / cosine	
Tilt range	± 60°	± 60°	± 66°
Tilt increment		2°	

952